Cardiac patches made of brown adipose-derived stem cell sheets and conductive electrospun nanofibers restore infarcted heart for ischemic myocardial infarction

Xinbo Wei [a,1], Li Wang [a,1], Cuimi Duan [b], Kai Chen [a], Xia Li [c], Ximin Guo [b,***], Peng Chen [d,**], Haifeng Liu [a,*], Yubo Fan [a]

[a] *Key Laboratory for Biomechanics and Mechanobiology (Beihang University) of Ministry of Education, Beijing Advanced Innovation Center for Biomedical Engineering, School of Biological Science and Medical Engineering, Beihang University, Beijing, 100083, PR China*
[b] *Department of Advanced Interdisciplinary Studies, Institute of Basic Medical Sciences, Beijing, 100850, PR China*
[c] *Beijing Citident Stomatology Hospital, Beijing, 100032, PR China*
[d] *Department of Ultrasound, The Third Medical Center, Chinese PLA General Hospital, Beijing, PR China*

ARTICLE INFO

ABSTRACT

Cell sheet engineering has been proven to be a promising strategy for cardiac remodeling post-myocardial infarction. However, insufficient mechanical strength and low cell retention lead to limited therapeutic efficiency. The thickness and area of artificial cardiac patches also affect their therapeutic efficiency. Cardiac patches prepared by combining cell sheets with electrospun nanofibers, which can be transplanted and sutured to the surface of the infarcted heart, promise to solve this problem. Here, we fabricated a novel cardiac patch by stacking brown adipose-derived stem cells (BADSCs) sheet layer by layer, and then they were combined with multi-walled carbon nanotubes (CNTs)-containing electrospun polycaprolactone/silk fibroin nanofibers (CPSN). The results demonstrated that BADSCs tended to generate myocardium-like structures seeded on CPSN. Compared with BADSCs suspension-containing electrospun nanofibers, the transplantation of the CPSN-BADSCs sheets (CNBS) cardiac patches exhibited accelerated angiogenesis and decreased inflammation in a rat myocardial infarction model. In addition, the CNBS cardiac patches could regulate macrophage polarization and promote gap junction remodeling, thus restoring cardiac functions. Overall, the hybrid cardiac patches made of electrospun nanofibers and cell sheets provide a novel solution to cardiac remodeling after ischemic myocardial infarction.

1. Introduction

Ischemic myocardial infarction (MI), which is resulted from an interruption of blood supply, accounts for the majority of diseases and death [1–3]. The current therapeutic principle for MI is targeted to protect and maintain heart function, save dying myocardium and prevent the expansion of the infarct area [4]. However, the limited proliferation of native cardiomyocytes and concomitant inflammatory responses frequently lead to fibrous remodeling and heart failure [5–7]. Generally, effective treatments for MI require the introduction of

functional cargoes, such as the injection of living cells, proteins, and genes [8]. In-time renovation of cardiomyocytes is of great importance for treating MI. To date, stem cell-based therapies have emerged as up-and-coming solutions for various intractable diseases, including acute MI [9–11]. However, the low cell retention after injection yet challenges the therapeutic efficiency of stem cell therapy.

In recent years, artificial cardiac patches have shown promising potential in delivering therapeutics for myocardial regeneration, thus promoting heart tissue remodeling [5,12,13]. As an example, human induced pluripotent stem cell-derived cardiac muscle patches with
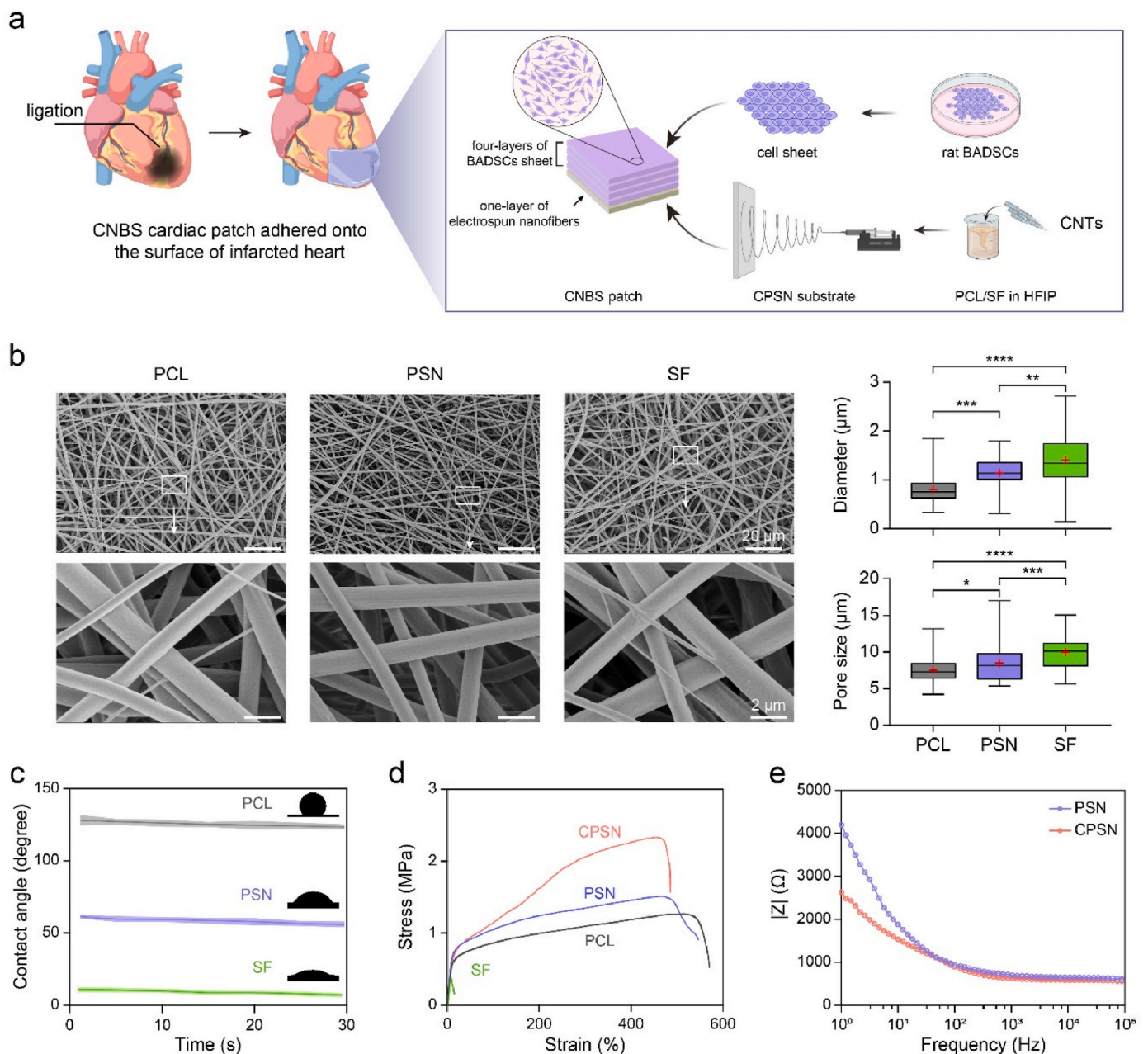

Fig. 1. Development of CNBS cardiac patches in this study. (a) Schematic illustration of the fabrication of CNBS cardiac patches and application for the treatment of MI. (b) Representative microstructures of PCL nanofibers, PSN, and SF nanofibers observed by SEM, and the diameter and pore size were quantified with a 95% confidence interval (red "+" denoted the mean value; boxes showed minimum value, median value, interquartile range and maximum value). (c) The water contact angle of PCL nanofibers, PSN, and SF nanofibers. (d) Stress-strain curves of PCL nanofibers, PSN, SF nanofibers, and CPSN. (e) The EIS of bare PSN and CPSN in PBS. *, $p < 0.05$; **, $p < 0.01$; ***, $p < 0.001$; ****, $p < 0.0001$ according to one-way ANOVA followed by LSD post-hoc test (e). Fifty electrospun nanofibers and pores were counted (e).

clinically relevant size were fabricated for treating MI [14]. This cardiac muscle patch not only significantly reduced the infarct size but also improved cardiac function. Compared with directly seeding cells onto biomaterial surfaces and cell-encapsulated artificial scaffolds, cell sheet engineering holds more advantages as cardiac patches, including accelerated cardiomyogenesis, integrated extracellular matrix, and more powerful paracrine effects [6,15]. Besides, clinical trials have confirmed that cell sheets transplantation led to a better prognosis than cell solution therapy [16]. By applying a cell-involved cardiac patch on the surface of the heart, groups of paracrine factors derived from stem cells can facilitate endogenous repair of the infarcted myocardium [17, 18]. Interestingly, a previous study has verified that the four-layer cell

sheet constructs displayed long-term survival in athymic rats [19].

Adipose tissue is a storage depot that is abundant in stem cells [20, 21]. Preclinical data have suggested that pericardial adipose tissue released cytokines and growth factors to regulate ventricular function in response to MI [22]. Adipose-derived stem cells (ADSCs) have also been recognized to show great promise for the treatment of MI [23]. ADSCs have a strong potential to differentiate into cardiomyocyte-like cells upon direct cell-to-cell interaction with native cardiomyocytes and secrete factors derived from those cardiomyocytes. In this regard, ADSCs-based patches can remodel infarcted heart by restoring blood circulation [24], modulating the immune microenvironment [25], and renovating cardiomyocytes [26]. In general, there are two categories of

ADSCs, white ADSCs (WADSCs) and brown ADSCs (BADSCs), existing in mammals. Previous studies have confirmed a stronger pluripotent capacity of BADSCs than WADSCs and, unlike other stem cells, BADSCs can spontaneously differentiate into cardiomyocytes without the addition of 5-azacytidine [27,28].

However, the successful applications of cell sheets are hampered by two main obstacles in the treatment of MI. First, an ideal cardiac patch requires suitable mechanical support to match the native heart [29]. Interestingly, biomaterial-based substrates can also serve as patches to deliver therapeutic molecules and provide mechanical support. Silk fibroin (SF), a natural biomacromolecule, has attracted wide interest in tissue engineering due to its biocompatibility, biodegradability, morphologic flexibility, and a number of tangible mechanical properties [30]. Recently, SF has been demonstrated as a potential alternative to induce the reprogramming and conversion of rat quiescent ventricular cardiomyocytes to pacemaker cardiomyocytes without affecting transcription factors [31]. Second, it is important for artificial patches to conduct electricity to connect the healthy myocardium and infarcted region, thus rebuilding damaged heart tissues [32,33]. Recent studies have focused on incorporating conductive materials into cardiac patches to enhance the synergistic capacity with adjacent cells [34]. Compared with other nanomaterial platforms such as graphene oxide and metallic nanoparticles, the outstanding conductivity and stability make carbon nanotubes (CNTs) exceptional for reconstructing cardiac tissues [35,36]. It has been shown that superaligned CNTs-laid poly (dimethylsiloxane) substrate not only induced an aligned cardiomyocyte morphology but also created an electrical signal transmission pathway [37]. Therefore, we hypothesized that CNTs-incorporated electrospun nanofibers could both establish electrical connection among isolated cells and promote the remodeling of the infarcted myocardium.

As shown in Fig. 1a, we proposed a new kind of multilayered cardiac patch consisting of CNTs-incorporated electrospun polycaprolactone (PCL)/SF nanofibers (CPSN) and BADSCs sheets. By blending PCL with SF, we assumed that mechanical properties of the electrospun polycaprolactone (PCL)/SF nanofibers (PSN) could be remarkably modified [38,39], and that the PSN could reserve the ability to promote the differentiation of BADSCs towards cardiomyocytes and the maturation of the existed cardiomyocytes. In this study, we first characterized the morphology, mechanical property, hydrophilicity and electrochemical impedance of CPSN. Next, we confirmed that the CPSN could promote cardiomyogenic differentiation of the primary BADSCs. From both in vivo and in vitro experiments, we demonstrated the CPSN/BADSCs sheets (CNBS) cardiac patches could accelerate myocardial remodeling of MI rats by promoting angiogenesis, moderating inflammation, and enhancing cardiomyocyte renewal.

2. Experimental sections

2.1. Isolation and confirmation of primary rat BADSCs

Primary BADSCs were isolated from Sprague Dawley rats (male, 4 weeks; Beijing Vital River Laboratory Animal Technology Co., Ltd.) using a well-established method [40]. In brief, brown adipose depots were isolated from the scapula of rats. These tissues were washed with cold Dulbecco's phosphate buffered solution (DPBS, Solarbio, China), gently minced using small scissors, and then digested with a mixed digestive enzyme solution (PBS containing 0.05% trypsin, 0.1% collagenase IV, and 0.1% Dispase II) at 37 °C for 40 min. Next, cells were filtered through a 200-mesh strainer and centrifuged at $600 \times g$ for 8 min. The cell pellet was resuspended in Minimum Essential Medium-α (α-MEM, Thermo Fisher Scientific, USA) and counted using a hemocytometer. The freshly primary BADSCs (P0) were used for experiments. The isolated cells were inoculated into normal Petri dishes (as control), PSN-plated Petri dishes, and CPSN-plated Petri dishes with media changed every day in the first three days, and every two days afterward.

Immunocytofluorescence (ICF) staining (see section 2.12) was used

to confirm the isolated BADSCs, the cells after three times of media changes were stained against CD90 (1:300; NB100-65543; Novus) and UCP-1 (1:200; GB112174; Servicebio) antibodies. For flow cytometry analysis, about one million cells were trypsinized, collected and fixed with 2% paraformaldehyde (PFA, Solarbio, China) for 20 min. After incubating with flow cytometry buffer (Thermo Fisher Scientific, USA) for 30 min, the cells were respectively stained against FITC-CD29 (1:100; 14-0291-82; Invitrogen) and FITC-CD44 (1:50; MA1-81319; Invitrogen) antibodies for 30 min at 4 °C. Then the cells were washed with PBS and detected using a flow cytometry (BD LSRFortessa SORP, BD Biosciences). Tri-lineage differentiation was also carried out. After three passages, the isolated cells were cultured in osteogenesis, adipogenesis, or chondrogenesis induction media (ADRS-D101, ADRS-D102, ADRS-D203; Haixing Biosciences, China) in accordance with the manufacturer's instructions. Osteogenic, adipogenic, and chondrogenic differentiation was separately confirmed by alkaline phosphatase staining (C3206; Beyotime, China), Oil red O staining (G1262; Solarbio, China), and Alcian Blue staining (Haixing Biosciences, China) after 7 days of induction. The images were taken by using an optical microscope (Nikon Eclipse TE2000-U Kanagawa, Japan).

2.2. Preparation of BADSCs sheet

Three hundred thousand BADSCs were seeded into a PIPAAm-coated 6-well plate (174,901; Thermo Fisher Scientific, USA) and incubated at 37 °C. After 10 days of culture, the plate was moved to room temperature for 1 h, then cells were collected in the form of a monolayered cell sheet. H&E staining was conducted to observe the BADSCs sheet.

2.3. Fabrication of conductive CPSN

Regenerated silk fibroin was prepared as described in previous reports. Briefly, natural silk was boiled in sodium carbonate solution (Na_2CO_3 in DIW, 0.02 M) for 30 min and then washed with boiling DIW. Sericin was fully removed after five boiling and washing cycles. Then, the degummed silk fibers were dissolved in lithium bromide (LiBr in DIW, 9.3 M) at 60 °C for 4 h. After centrifugation at 8000 rpm for 20 min, the supernatant was dialyzed against DIW using a dialysis membrane (MWCO = 3.5 kDa). Finally, freeze-drying regenerated silk fibroin was acquired and stored under 4 °C until use.

To fabricate CPSN, PCL and SF were individually dissolved in hexafluoroisopropanol (HFIP) to acquire solutions with a concentration of 10 wt%. Next, a mixed solution was prepared by thoroughly blending PCL and SF compounds with different mass ratios (1:0, 1:1, 0:1). After that, CNTs (diameter, 20–30 nm; length, 10–30 μm; Beijing BOYU GAOKE, China) (10 mg/ml) were dispersed in the mixed PCL/SF solution by stirring for 1 h. Then, the electrospun nanofiber mats were acquired with the following parameters: voltage = 18 kV, needle tip-collector distance = 15 cm, solution flow rate = 2 ml/h. The obtained CPSN mats were immersed in 75% of alcohol for 30 min to allow the crosslinking of SF. Finally, the as-prepared CPSN was dried under vacuum at room temperature for 7 days.

2.4. SEM, contact angle, mechanical properties, and electrochemical measurements

The morphology of electrospun nanofiber mats was examined by SEM (ZEISS Gemini 300, USA). The dry mats were sputter coated with gold for 120 s. SEM micrographs of the dry mats were acquired and they were analyzed with ImageJ software (Version 1.8.0). The hydrophilicity of electrospun nanofibers was evaluated by the sessile drop method using a contact angle analyzer (Shanghai Powereach Digital Technology Equipment Co. Ltd., China). Four microliters of ultrapure water were dropped onto the surface of films at room temperature. The images were recorded continuously after water was contacted with the samples. The average contact angle was acquired from five independent repetitions.

Mechanical properties of electrospun nanofibers were detected using a uniaxial tensile tester (Instron 3344; Instron, Co. Ltd., UK) at room temperature. The electrospun nanofiber mats were cut into blocks with dimensions of $20 \times 10 \times 3$ mm. The tensile speed was set as 20 mm/min. Stress-strain curves were recorded for each type of electrospun nanofiber mats.

The impedance of electrospun nanofibers was measured with an electrochemical workstation (Autolab, Metrohm, Switzerland). The test samples ($10 \times 10 \times 3$ mm) were sandwiched between a conductive electrode and the solution groove. The electrochemical impedance spectroscopy (EIS) was acquired in PBS buffer, with frequency ranging from 100 kHz to 1 Hz.

2.5. Cell viability

BADSCs were seeded into a 96-well plate and allowed to adhere for overnight. At determined timepoints, the culture media was replaced with fresh media containing the CCK-8 agent (10 v/v%). After incubation for another 2 h, the absorbance at 450 nm was measured with a microplate reader (Thermo Fisher Scientific, USA).

2.6. Tube formation assay

Primary human umbilical vein endothelial cells (HUVECs) were isolated from human umbilical cord veins (People's Hospital of Peking University, China) as previously reported [41]. To start with, a CNBS patch conditioned medium (CNBS-CM) was prepared. The CNBS patch was minced and transferred into an endothelial cell medium (ECM; Sciencell, USA) with 10% fetal bovine serum (FBS; Sciencell, USA). After incubating at 37 °C for 24 h, the mixture was centrifugated at $1000 \times g$ for 10 min at 4 °C to pellet the patch fragments. Next, the supernatant was retrieved and filtered using a 0.22 μm filter membrane. HUVECs were seeded into a Matrigel (Corning, USA) coated 96-well plate. Four hours later, tube formation was photographed with an optical microscope and analyzed with the "Angiogenesis Analyzer" plugin in ImageJ software.

2.7. Scratch wound assay

One hundred and fifty thousand HUVECs were seeded into a 24-well plate and were allowed to reach 90% confluency overnight. A scratch was created using a 200 μl pipette over the cell monolayer and photographed. After 24 h and 48 h of culture, the same positions were photographed again. The wound area was measured with ImageJ software. Three non-overlapping regions were recorded per well.

2.8. Transwell migration assay

HUVECs were seeded in the transwell upper chamber at a density of 5×10^5 cells/ml and allowed to settle down. Then, 600 μL of ECM or CNBS patch CM was carefully added to the bottom of the lower chamber in a 24-well plate. After incubation for the indicated times, the transwell inserts were removed from the plate and washed with PBS three times. Following removing the remaining cells on the top of the membrane using a cotton swab, these inserts were immersed in 4% PFA for 10 min and stained with crystal violet solution (0.1 wt%). Then the migrated cells were photographed and analyzed with ImageJ software.

2.9. Animals and transplantation of patches

Sprague Dawley rats (male, 270–350 g) were purchased from the experimental animal center of the Beijing Academy of Military Medical Sciences. The animal experiments received approval from the animal ethics committee of Beihang University (Approval number: BM20200059). All animals were cared for following the guidelines of the National Institutes of Health. The MI rat model was developed as per

the previous study [12]. In brief, the rats were anesthetized by intraperitoneal injection of sodium pentobarbital (2 wt%) at a dose of 30 mg/kg. After shaving off the fur, the rat hearts were exposed by left thoracotomy, and acute MI was induced by ligation of the left anterior descending coronary artery with a 6-0 suture. The successful establishment of rat MI was confirmed by ECG detection. The rats were randomly divided into four groups (n = 3 for each group): (i) sham group (without MI injury), (ii) MI without further treatments (no-treatment control group), (iii) MI with CPSN and BADSCs suspension treatment (PSN-sus group; 6×10^6 cells in total; in 50 μl PBS), the cell suspension was administrated via intramyocardial injection with the CPSN placed on the surface of rat hearts, and (iiii) MI with CNBS cardiac patch treatment (CNBS group; 1.5×10^6 cells/sheet; four layers of cell sheets in total), the CNBS patch was placed on the rat hearts with CPSN on the outside. The corresponding PSN-sus or CNBS patch was transplanted and adhered to the infarcted heart area. Finally, the wounds were sutured and the rats were allowed to recover. At the end of the experiment, the rat serum was collected by centrifuging whole blood at $1000 \times g$ for 20 min at 4 °C. The serum was used for enzyme-linked immunosorbent assay (ELISA) to detect inflammatory cytokines IL-8, TNF-α and IL-10 (SEKR-0014, SEKR-0009 and SEKR-0006; Solarbio, China) according to the manufacturer's instructions.

2.10. Echocardiography

Four weeks post-surgery, the rats were anesthetized by intraperitoneal injection of sodium pentobarbital (2 wt%). A medical imaging expert who was blinded to the experimental design manipulated the doppler ultrasound machine (Vevo2100, FUJIFILM VisualSonics Inc., USA). The 2D images were collected and the corresponding parameters including left ventricular ejection fraction (LVEF), left ventricular fraction shortening (LVFS), end diastolic volume (EDV), and end systolic volume (ESV) were recorded.

2.11. Cell stability in vivo

Fluorescent probe DiD (Beyotime, China) was used to label BADSCs for in vivo stability assay. Before transplantation, the BADSCs sheet or BADSCs suspension was incubated with 20 μM DiD for 2 hous followed by rinsing with PBS 3 times. The rats were anesthetized by intraperitoneal injection of sodium pentobarbital (2 wt%). At determined timepoints, images were taken and analyzed with in vivo imaging system (IVIS Lumina III, PerkinElmer, USA).

2.12. Histology and immunostaining

The rat heart tissues were harvested after vascular perfusion with normal saline. For Masson's staining and elastin staining, paraffin-embedded heart tissues were cut into sections with a thickness of 5 μm. The sections were then rehydrated and stained using the corresponding staining kits (G1346, and G1593; Solarbio, China) following the manufacturer's instructions. They were subsequently mounted with neutral balsam and photographed with an optical microscope (Nikon Eclipse TE2000-U Kanagawa, Japan).

For immunohistochemistry (IHC) and immunohistofluorescence (IHF) staining, rat tissue cryosections were rinsed with PBS and fixed with 4% PFA. Antigen retrievals were conducted in citrate buffer at 100 °C for 20 min. After that, the sections were permeabilized and blocked with a 5% BSA blocking buffer (Solarbio, China) containing 0.25% Triton X-100 (MedChemExpress, USA) for 1 h at room temperature. The following primary antibodies were incubated with sections overnight at 4 °C: anti-CD45 (1:200; NB100-77417; Novus), anti-CX43 (1:100; #3512; Cell Signaling Technology), anti-α-actinin (1:100; #6487; Cell Signaling Technology), anti-Ki67 (1:100; ab15580; Abcam), anti-cTnT (1:100; ab209813; Abcam), anti-CD68 (1:100; ab28365; Abcam), anti-CD34 (1:200; ab881289; Abcam), anti-α-SMA (1:500;
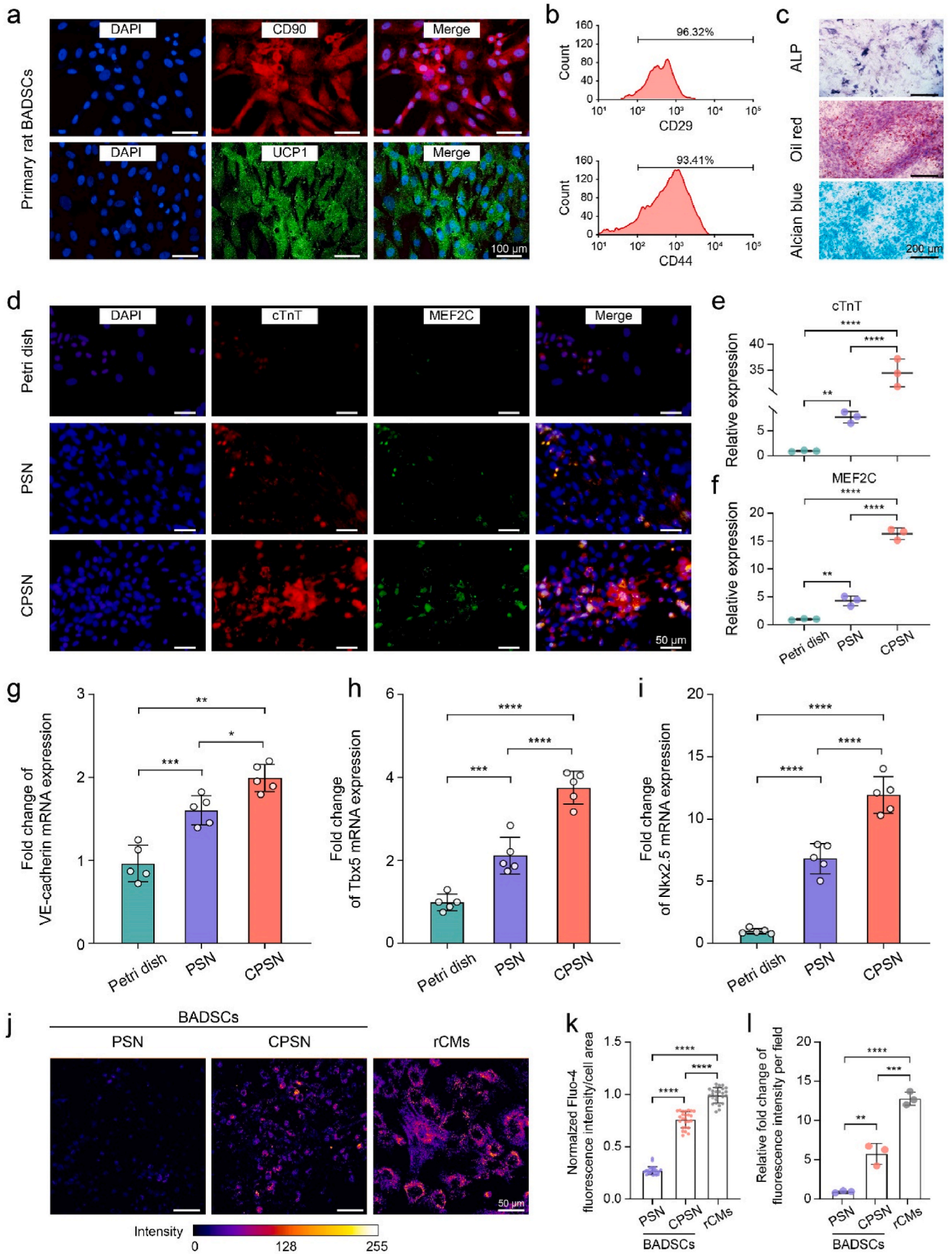
(caption on next page)

Fig. 2. CPSN substrate supported the differentiation of primary BADSCs towards cardiomyocytes. (a) Immunostaining images showing the specific markers CD90 and UCP1 of BADSCs. (b) Flow cytometry analysis showing the surface markers CD29 and CD44 of the isolated BADSCs. (c) Representative images showing the tri-lineage differentiation capacity of the primary BADSCs. (d–f) Representative immunofluorescent images showing the expression of MEF2C and cTnT, and the relative fluorescence intensity was quantified accordingly. (g–i) RT-PCR analysis showing the expression level of cardiomyogenesis-related genes VE-cadherin, T-box transcription factor 5 (Tbx5), and NK2 homeobox 5 (Nkx2.5). (j–l) Representative pseudo-color images showing Fluo-4 fluorescence intensity in BADSCs cultured on CPSN and PSN and in rCMs, and the fluorescence intensity was quantified accordingly. *, $p < 0.05$; **, $p < 0.01$; ***, $p < 0.001$; ****, $p < 0.0001$ according to one-way ANOVA followed by LSD post-hoc test (e-i, k, and l). All data were shown as mean $\pm$ SD. Values of independent experiments were: $n = 3$ (e, f and l), 5 (g–i). Twenty-five individual cells were counted (k).

#19245; Cell Signaling Technology) antibodies. For IHF staining, secondary antibodies conjugated with Alexa Fluor 594 (1:400; ab150080; Abcam) or Alexa Fluor 488 (1:400; ab150117, ab150113; Abcam) were incubated with the sections on the next day for 1 h. DAPI (Solarbio, China) was used for nuclear counterstaining. Fluorescent images were taken using a confocal microscopy (Leica Microsystems GmbH, Mannheim, Germany). For IHC staining, horseradish peroxidase-conjugated goat anti-rabbit IgG (1:1000; ab6721; abcam) were incubated with the sections for 1 h. Then, DAB (3,3′-Diaminobenzidine) substrate was used to visualize the positive region, and hematoxylin was used to counterstain nuclear. Images were taken with an optical microscope (Nikon Eclipse TE2000-U Kanagawa, Japan). The quantification was conducted using ImageJ software.

For ICF staining, the cultured cells were washed with PBS, fixed with 4% PFA for 15 min, and permeabilized with 0.25% Triton X-100 for 30 min. After blocking with 5% goat serum (SL08; Solarbio) for 1 h, primary anti-MEF2C (1:100; ab118406; abcam) and anti-cTnT (1:100; ab209813; Abcam) antibodies were incubated with the cells at 4 °C for overnight. Then, the cells were washed with PBS for three times and incubated with secondary antibodies at room temperature for 1 h. FITC-phalloidin was also used to visualize F-actin. The staining was observed using Dragonfly high speed confocal microscope (Dragonfly 200, ANDOR, Oxford Instruments).

2.13. RT-PCR

Total RNA was collected from the infarcted rat hearts. Complementary DNA (cDNA) was produced using PrimeScript™ RT Master Mix (Takara, Japan). Quantitative real-time PCR (RT-PCR) was performed with Thermal Cycler Dice™ Real Time System (Takara, Japan). The relative expression of the interested genes was calculated using the $2^{-(\Delta\Delta ct)}$ method and normalized to GAPDH. All primers were synthesized by Sangon Biotech (Shanghai, China), and listed in Table s2.

2.14. Western blotting

The rat hearts were ground and homogenized in ice-cold RIPA lysis (15 mg:1 ml; Solarbio, China). After centrifugation at $13,000 \times$ for 20 min at 4 °C, the supernatant was collected for use. The protein concentrations were quantified by using BCA protein assay kit (PC0020; Solarbio, China). Then, each protein sample was denatured at 96 °C for 10 min, separated by using 10% SDS-PAGE gels (AR0138; Boster, China) and transferred to polyvinylidene fluoride (PVDF) membranes (Millipore, USA). The membranes were then blocked by using 5% non-fat milk (Beyotime, China) for 1 h at room temperature followed by incubation with the following primary antibodies at 4 °C for overnight: anti-Cleaved caspases 3 (1:1000; A19654; ABclonal), anti-Caspase-3 (1:1500; ab184787; Abcam) antibody, and anti-β-actin (1:1000; AC006; ABclonal). After washing with Tris-buffered saline with 0.1% Tween 20 (TBST, T1081; Solarbio, China) for 3 times, the membranes were incubated with HRP-conjugated goat anti-rabbit IgG (BA1054; Boster, China) for 1 h at room temperature. Finally, the membranes were washed with TBST for 5 times and visualized by using chemiluminescence (ECL, AR1172; Boster, China).

2.15. Statistics

Scatters in the bar indicate the values of independent experiments. Data were shown as mean $\pm$ standard deviation (SD). Statistical significance between groups was calculated with IBM SPSS Statistics software (version 25.0). Two-tailed unpaired *t*-test was used to compare the mean of two independent groups. One-way ANOVA followed by Least Significance Difference (LSD) post-hoc test (compare the mean of each column with the mean of every other column) was used for comparisons among multi-groups within one dataset. Scatters in each bar graph indicated the values of independent experiments. $p < 0.05$ was considered statistically significant. ns, $p > 0.05$; *, $p < 0.05$; **, $p < 0.01$; ***, $p < 0.001$; ****, $p < 0.0001$.

3. Results

3.1. Fabrication and characterization of CPSN

The fabrication strategy of CNBS cardiac patches is illustrated in Fig. 1a. In brief, PSN was first prepared from a mixture of PCL and SF (weight ratio of 1:1) dissolved in HFIP via electrospinning. The hybrid nanofibers were collected with a piece of tinfoil (Figure s1 tables1 and s2). The prepared PSN presented an average nanofiber diameter of 1.156 $\pm$ 0.296 μm, which was larger than that of PCL nanofibers (0.807 $\pm$ 0.264 μm) but smaller than that of SF (1.411 $\pm$ 0.629 μm) nanofibers. The average pore sizes of PCL, PSN and SF nanofibers were 7.563 $\pm$ 1.873 μm, 8.484 $\pm$ 2.399 μm, and 10.010 $\pm$ 1.950 μm respectively (Fig. 1b and Table s1). Compared with PCL nanofibers, the addition of regenerated SF also improved the surface hydrophilicity of electrospun nanofibers (final water contact angle: 124.47 $\pm$ 1.42° in PCL nanofibers, 54.38 $\pm$ 1.58° in PSN and 5.60 $\pm$ 0.55° in SF nanofibers) (Fig. 1c). For fabricating CPSN, CNTs were mixed with the PCL/SF solution prior to electrospinning. Mechanical properties of the nanofibers were detected through the tensile tests. The stress-strain curves showed that compared with PCL nanofibers, PSN demonstrated slightly increased tensile strength and decreased elongation at break due to the incorporation of relatively fragile SF (Fig. 1d and Table s1) [42,43]. When CNTs were added, the maximum stress (1.66 $\pm$ 0.14 MPa for PSN compared with 2.40 $\pm$ 0.11 MPa for CPSN) of the electrospun substrate was significantly increased while the breaking elongation (529.48 $\pm$ 19.50% for PSN compared with 486.60 $\pm$ 18.09% for CPSN) was decreased. To better elicit the incorporation of CNTs, the electrical properties of electrospun nanofibers were evaluated by comparing their electrical impedance against frequency. At low frequency, the CPSN showed lower electrical impedance than bare PSN (Fig. 1e), indicating that electrical conductivity of the PSN was significantly enhanced by incorporating CNTs.

3.2. Differentiation of primary BADSCs cultured on CPSN

The results of ICF staining showed that the primary BADSCs presented CD90 and uncoupling protein 1 (UCP1) positive phenotypes (Fig. 2a). UCP1 is responsible for generating heat through non-shivering thermogenesis, a specialized function of brown adipocytes, which distinguishes BADSCs from their counterparts such as WADSCs [44]. The positive expressions for stem cell surface markers CD29 (96.32 $\pm$ 2.34%) and CD44 (93.41 $\pm$ 2.13%) were also confirmed by flow
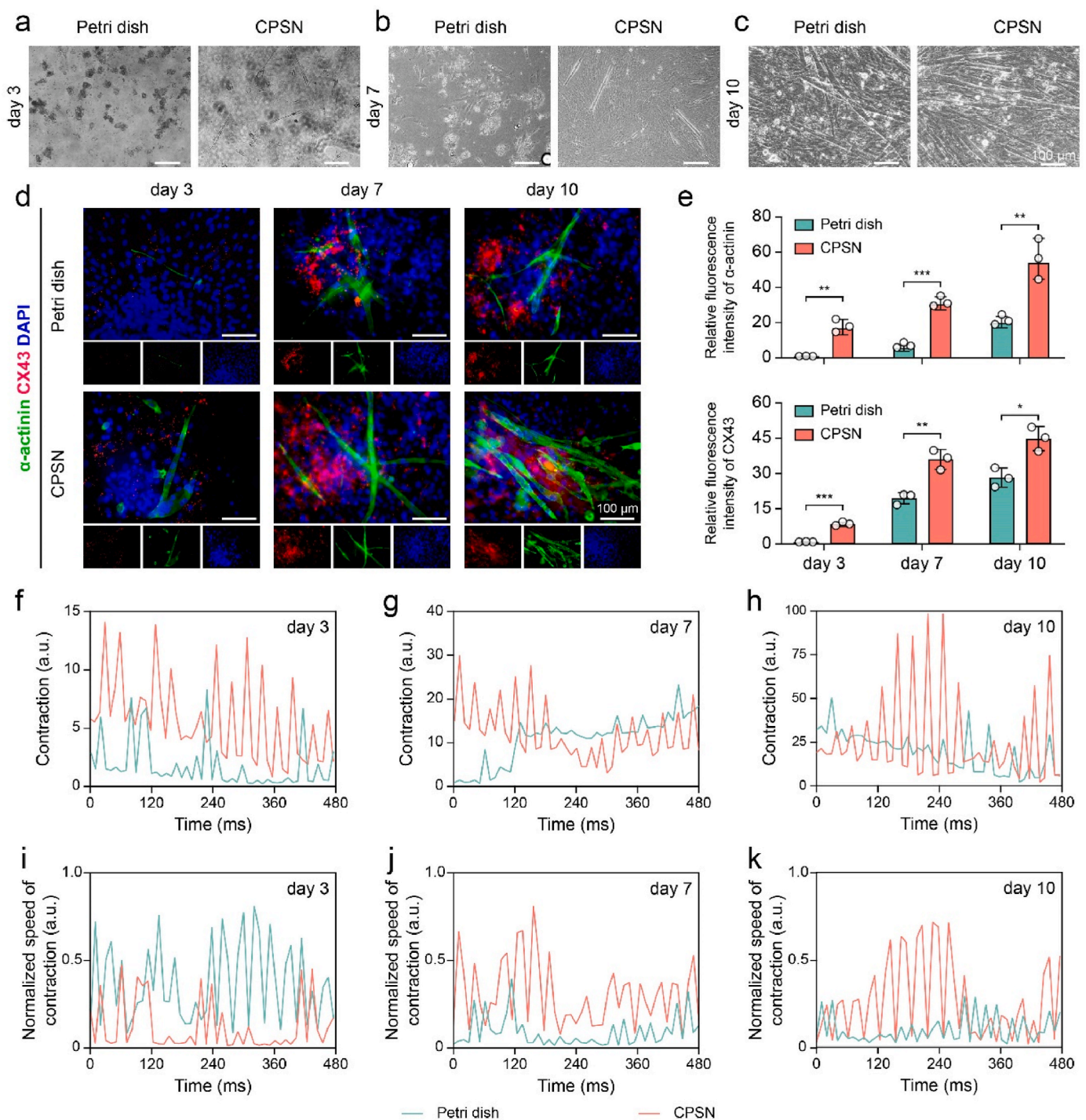
Fig. 3. CPSN substrates promoted the differentiation of BADSCs towards beating cardiomyocytes. (a–c) Optical images showing BADSCs seeded on Petri dishes and CPSN at (a) day3, (b) day 7, and (c) day 10. (d) Representative confocal images showing the differentiation of BADSCs. (d) Quantification of α-actinin (green) and CX43 (red) fluorescent intensity. (f–h) Time course profile of the contraction calculated with the "MUSCLEMOTION" plugin in ImageJ software. (i–k) The normalized speed of contraction was determined accordingly. *, $p < 0.05$; **, $p < 0.01$; ***, $p < 0.001$ according to two-tailed *t*-test at each time point (e). All data were shown as mean $\pm$ SD. Value of independent experiments was: n = 3 (e).

cytometry (Fig. 2b). Meanwhile, the isolated BADSCs exhibited capacities for osteogenesis, adipogenesis and chondrogenesis which were verified by ALP staining, Oil red O staining and Alcian blue staining respectively (Fig. 2c). These results suggested the successful isolation of rat primary BADSCs.

Regenerated SF has been reported to facilitate the formation of macromolecular structures in extracellular matrix environment [45]. More importantly, it was recently found that SF could induce the ectopic

expression of VE-cadherin in quiescent cardiomyocytes to drive their conversion towards pacemaker cardiomyocytes [31]. Therefore, we explored whether the CPSN substrates improved the cardiomyogenesis of BADSCs. Firstly, we showed the same trend of VE-cadherin expression in BADSCs cultured on different surfaces, of which CPSN significantly upregulated VE-cadherin expression compared with PSN (Figure s3). The BADSCs cultured on Petri dish exhibited an irregular distribution, while they presented an elongated cell morphology when cultured on
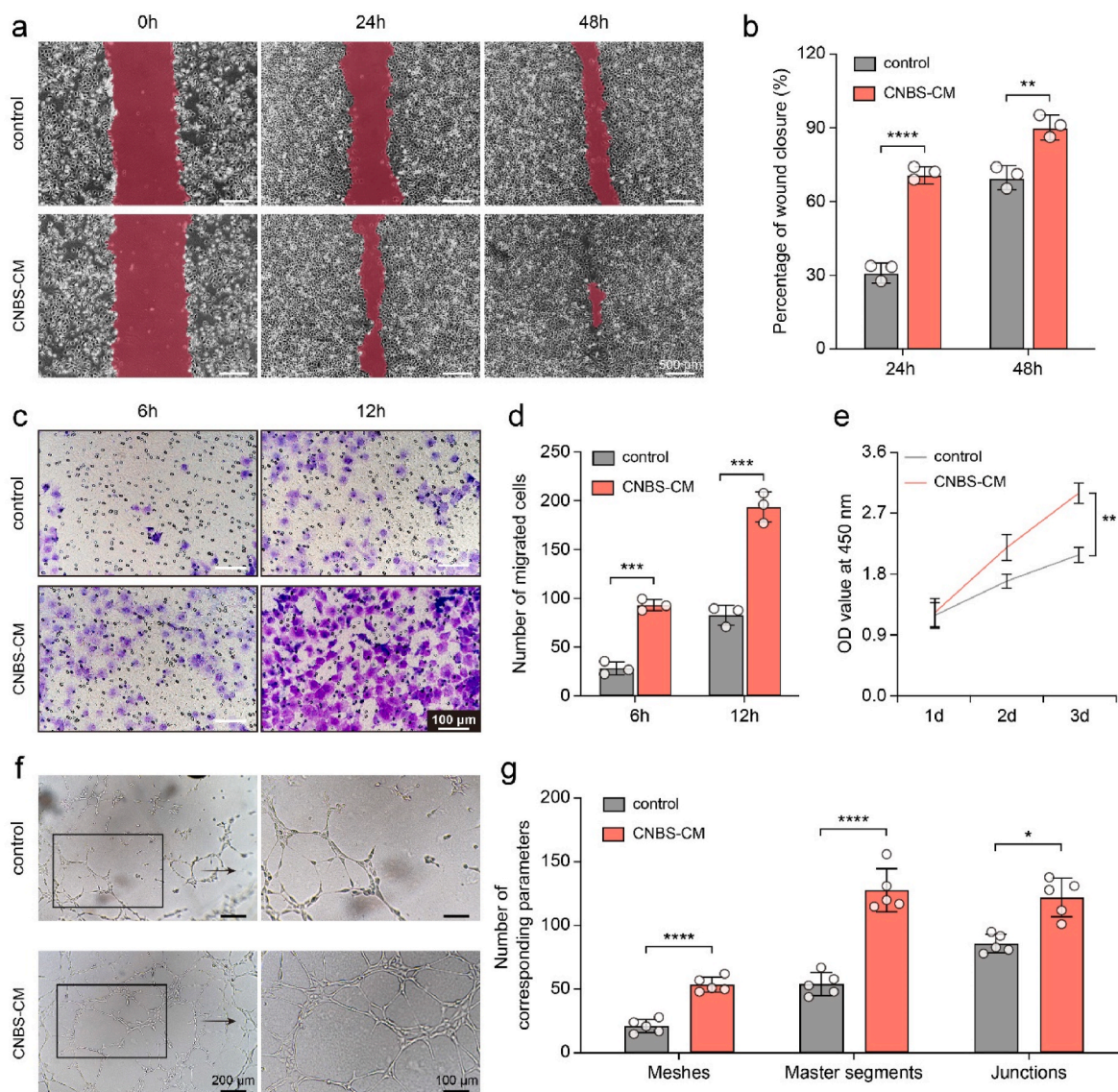
Fig. 4. In vitro activities of CNBS cardiac patches. (a and b) Wound scratch assay upon treatment of control and CNBS-CM, and the quantitative results. (c and d) transwell chamber migration for control and CNBS-CM, and the number of migrated cells. (e) OD value at 450 nm of CCK-8 assays. (f and g) Tube formation assay upon treatment of control and CNBS-CM, and quantitative analysis with the "Angiogenesis Analyzer" plugin in ImageJ software. *, p < 0.05; **, p < 0.01; ***, p < 0.001; ****, p < 0.0001 according to two-tailed t-test at each time point (b, d, and e) and at each item (g). All data were shown as mean ± SD. Values of independent experiments were: n = 3 (b, d, and e), 5 (g).

PSN and CPSN surfaces at day 3 (Figure s4a). ICF staining revealed that cardiomyocyte marker cardiac troponin T (cTnT) was highly expressed in BADSCs cultured after three days. The CPSN substrate generated 11.17 ± 1.65% cTnT-positive cardiomyocytes, which was substantially higher than that of the PSN substrate (6.47 ± 0.54%) and Petri dish (3.27 ± 0.84%) (Fig. 2d, e and Figure s4b). Previous studies have reported that electrical conductivity was tightly linked to cardiac marker gene expressions [46]. Myocyte-specific enhancer factor 2C (MEF2C) is a representative marker of cardiac looping morphogenesis and is required for early cardiac differentiation in vitro [47]. Here, we observed the co-localization of MEF2C and cTnT in BADSCs. Moreover, the CPSN induced higher MEF2C expression in BADSCs compared with the PSN and Petri dish (Fig. 2d–f). As shown in Fig. 2g–i, the results of RT-PCR demonstrated that CPSN generated increased levels of VE-cadherin (relative mRNA levels: 1.00 ± 0.20 in control, 2.11 ± 0.39 in PSN, 3.75 ± 0.35 in CPSN), cardiac transcriptional factors Tbx5 (relative mRNA levels: 1.00 ± 0.18 in control, 1.66 ± 0.16 in PSN, 2.03 ± 0.15 in CPSN) and Nkx2.5 (relative mRNA levels: 1.00 ± 0.18 in

control, 6.86 ± 1.07 in PSN, 11.90 ± 1.30 in CPSN) compared to PSN. Next, we tested whether the incorporated CNTs affected intracellular calcium ions. As expected, the Fluo-4 fluorescence intensity indicated that the conductive CPSN induced a higher intracellular calcium flux and a broader calcium ion propagation in BADSCs than the bare PSN (Fig. 2j–k and Figure s5). Overall, these results suggested that the CPSN substrates improved the cardiac differentiation of rat primary BADSCs.

In light of the superior performances of CPSN, we also compared the effects of CPSN and Petri dish on inducing BADSCs towards functional cardiomyocytes. It was found that the BADSCs cultured on Petri dish exhibited an overall delayed differentiation process (Fig. 3a–c). And then, we conducted ICF staining to trace the differentiation of BADSCs at predetermined time points. The results showed that compared with Petri dish, CPSN effectively upregulated the expressions of α-actinin and connexin 43 (CX43) in BADSCs from the third day onwards (Fig. 3d and e). Besides, the CPSN induced more α-actinin -positive cells from day 3 onwards (1.06 ± 0.26% for Petri dish and 7.45 ± 1.24% for CPSN on day 3; 5.42 ± 0.72% for Petri dish and 17.73 ± 1.45% for CPSN on day
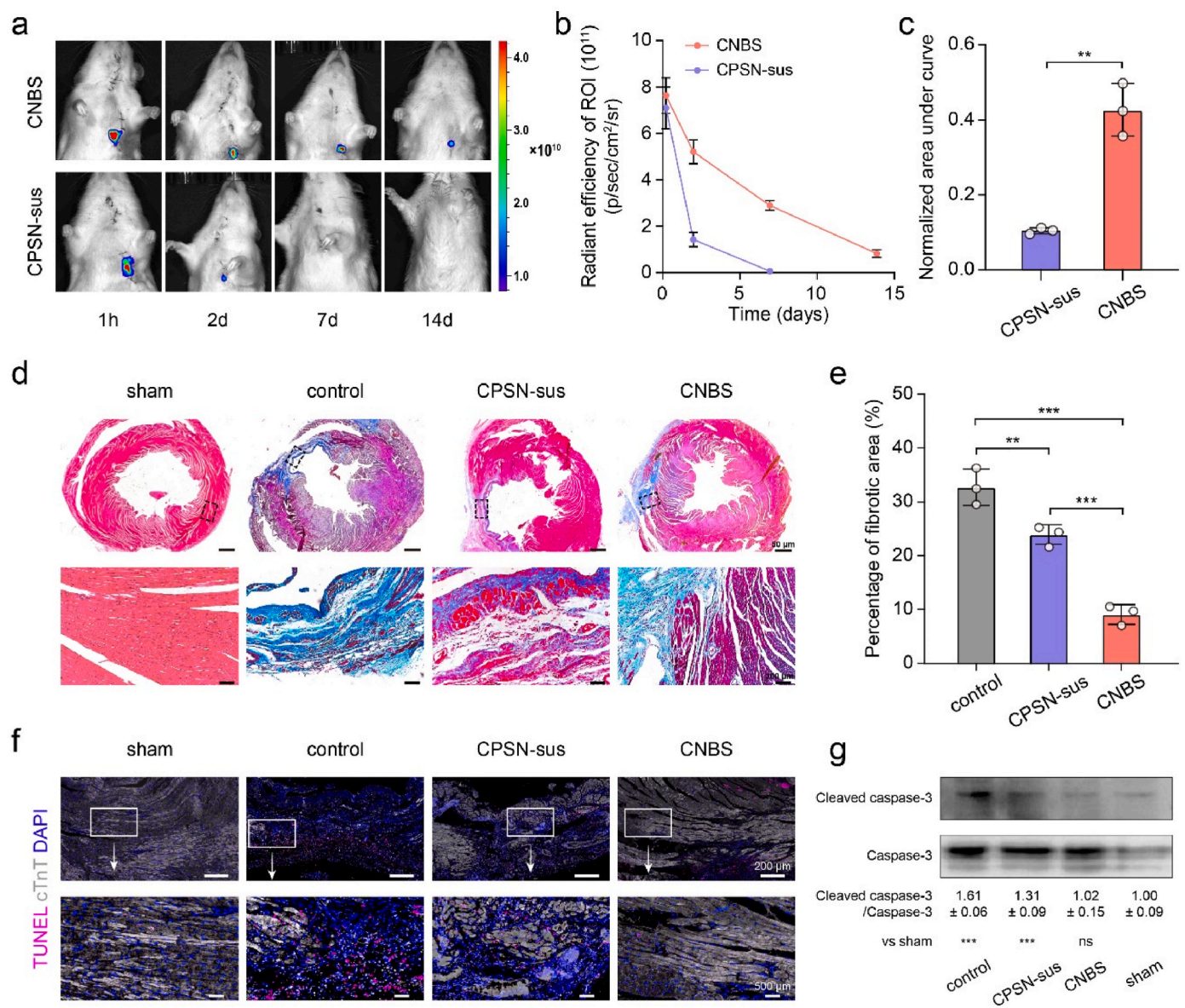
Fig. 5. CNBS patch increased cell retention and ameliorated cardiac damages in a rat MI model. (a–c) Fluorescent images of rats after transplantation of CNBS patch or PSN-sus, quantitative data of fluorescence intensity, and the normalized area under curves. (d and e) Masson's trichrome staining performed on paraffin-embedded heart sections, and the infarct size was calculated according to Masson's trichrome staining. (f) Representative images of TUNEL staining showing cardiomyocyte apoptosis. Below was the enlarged image of the upper one. (g) Immunoblots showing the expression of cell apoptosis-related protein Cleaved caspase-3 and Caspase-3 in rat hearts. The ratio of Cleaved caspase 3/Caspase 3 was normalized to sham. ns, $p > 0.05$; *, $p < 0.05$; **, $p < 0.01$; ***, $p < 0.001$; ****, $p < 0.0001$ according to two-tailed t-test (c) and one-way ANOVA followed by LSD post-hoc test (e and g). All data were shown as mean $\pm$ SD. Values of independent experiments were: n = 3 (c, e, and g).

7; 13.41 $\pm$ 1.21% for Petri dish and 31.34 $\pm$ 3.30% for CPSN on day 10) (Figure s6a). We also recorded videos to determine the contraction of BADSCs-differentiated cardiomyocytes. We found that both BADSCs cultured on Petri dish and CPSN-plated dish could contract spontaneously, and their contractions were further augmented over time. Moreover, the BADSCs were clustered and arranged in bundles after 10 days of culture, manifesting synchronous contraction (video s1-s6 and Figure s6b). By quantifying with MUSCLEMOTION [48], we demonstrated that the CPSN induced an enhanced beating characteristic for BADSCs (Fig. 3f–k). These results suggested that the functional cardiac differentiation of BADSCs was regulated by the CPSN substrates.

Supplementary video related to this article can be found at https://doi.org/10.1016/j.bioactmat.2023.03.023

3.3. In vitro biological activities of CNBS patch

We first prepared the BADSCs sheet by culturing the cells on a temperature-responsive cell culture surface. The acquired BADSCs sheet presented a diaphanous membrane with an average thickness of 227.43 μm (Figure s7a and b). We then fabricated CNBS cardiac patches by stacking four layers of BADSCs sheets and one layer of CPSN film. We used CNBS-derived conditioned media (CNBS-CM) to evaluate the biological activities. HUVECs cultured in CNBS-CM showed augmented migration in the scratch wound assay and transwell assay (Fig. 4a–d). The wound closure reached 72.67 $\pm$ 2.10% and 92.00 $\pm$ 3.68% after 24 h and 48 h of culture respectively in the CNBS-CM group, which was significantly higher than that in the control group (32.07 $\pm$ 2.82% and 71.11 $\pm$ 3.66% at the two timepoints respectively). Likewise, a larger number of cells migrated to the bottom of the transwell upper chamber
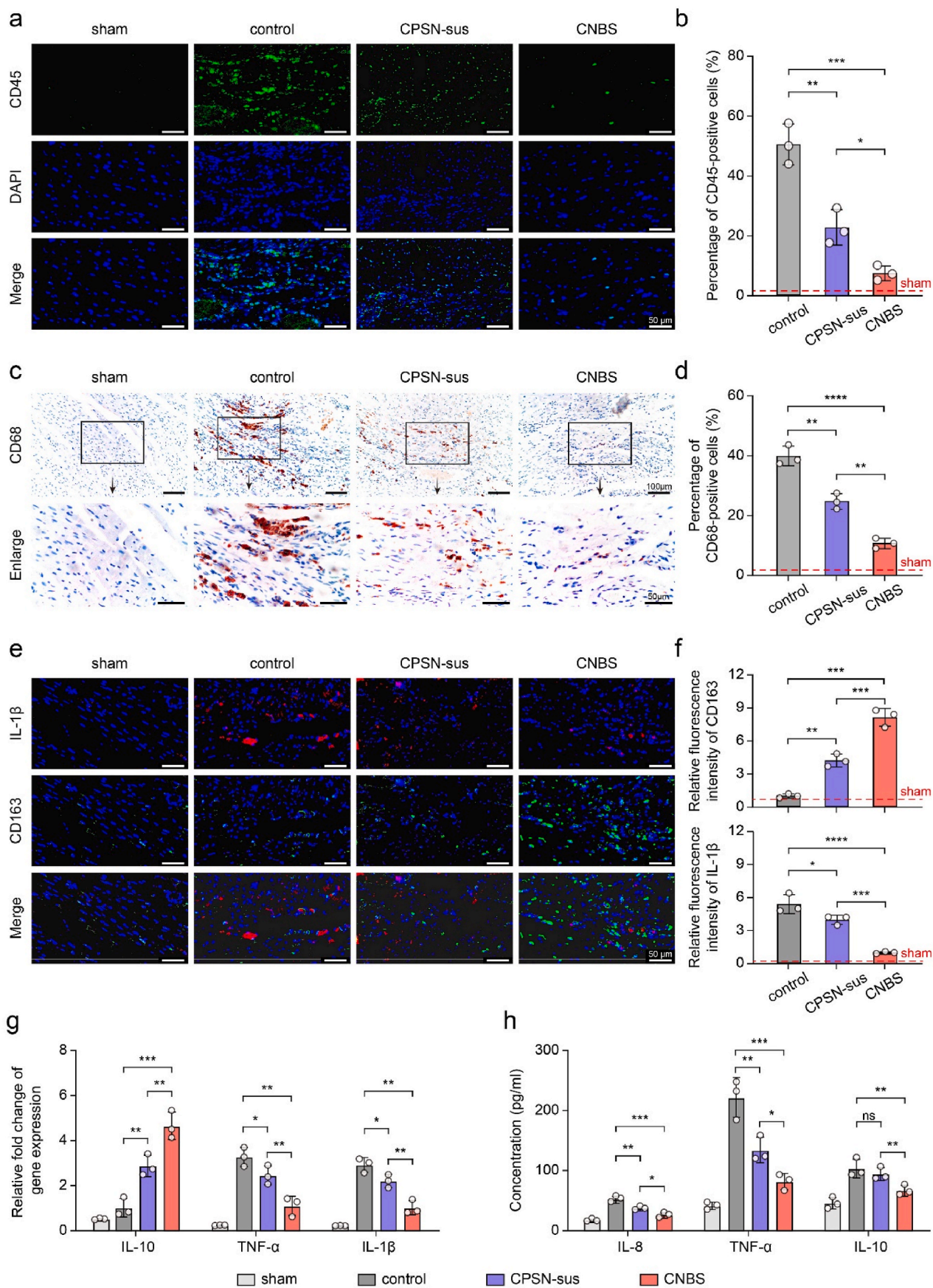
Fig. 6. CNBS patch modulated immune environment in vivo post MI. (a and b) Immunofluorescent staining images of CD45 (green) showing the leukocyte infiltration 4 weeks after transplantation and quantification of CD45-positive cells. (c and d) Representative IHC images of CD68 showing the infiltration of macrophages, and the quantification was conducted accordingly. (e and f) The reduction of pro-inflammatory IL-1β (red) and elevation of anti-inflammatory CD163 (green) were detected by IHF staining. g) The relative expression of inflammation-related mRNA was measured in the three groups via RT-qPCR. (h) The serum concentrations of inflammatory cytokines IL-8, TNF-α and IL-10 were detected by ELISA. For (a and e), the nucleus was counterstained by DAPI (blue). *, $p < 0.05$; **, $p < 0.01$; ***, $p < 0.001$; ****, $p < 0.0001$ according to one-way ANOVA followed by LSD post-hoc test (b, d, and f-h). All data were shown as mean ± SD. Values of independent experiments were: $n = 3$ (b, d, and f-h).

in the CNBS-CM group than in the control group. Meanwhile, the results of CCK-8 assay showed that all of the HUVECs, primary neonatal rat cardiomyocytes (rCMs) and BADSCs treated with CNBS-CM proliferated more quickly than the control (Fig. 4e and Figure s7c and d). Furthermore, the tube formation assay revealed that CNBS-CM increased the angiogenic capacity of HUVECs. After 4 h of culture, CNBS-CM treated HUVECs were able to form more endothelial meshes, segments and junctions compared to those cultured with normal ECM (Fig. 4f and g). Although we did not formally explore that whether the CPSN substrates influenced the cell behavior, these results suggested that CNBS patch held capacities to promote HUVECs migration, proliferation, and endothelial tube formation.

3.4. In vivo retention and prevention from myocardial infarction by CNBS treatment

Because the cardiac patch strategy can significantly improve cell retention, we transplanted DiD-labeled BADSCs into rat heart to study the in vivo stability. CPSN combined with BADSCs suspension (CPSN-sus) served as control. As shown in Fig. 5a, a strong fluorescence signal was found in both CNBS patch and CPSN-sus groups immediately after transplantation. The signal could not be detected after 7 days for CPSN-sus group, whereas it was detectable in the CNBS patch group even after 14 days of transplantation (Fig. 5b and c). These data suggested that CNBS patch resulted in a satisfied retention and stability of BADSCs around the heart. Masson's trichrome staining was then performed to analyze the cardiac fibrosis after 4 weeks of treatments. The results indicated that a large area of rat heart was damaged by ligation. CNBS patch transplantation promoted reduction of the infarcted region and decreased fibrotic area (Fig. 5d and e and Figure s8). To further detect the cardiac damage, the apoptotic cells were stained by using terminal deoxynucleotidyl transferase (TdT) dUTP nick-end labeling (TUNEL) staining. The CNBS-treated rat hearts (12.52 ± 1.17%) showed a significant reduction for cTnT/TUNEL double-positive cells compared with the rat hearts upon treatment with CPSN-sus (19.42 ± 2.06%) or no-treatment control (30.00 ± 2.72%) (Fig. 5f and Figure s9a). The cell apoptosis in rat hearts was also assessed by western blot assay. Cleaved caspase 3, the activated form of Caspase-3, will lead to the breakdown of myofibrillar proteins such as cTnT and α-actinin [49]. The immunoblots revealed a high ratio of Cleaved caspase 3/Caspase 3 in MI-injured rat hearts, which was significantly decreased by CNBS treatment (normalized ratio of Cleaved caspase 3/Caspase 3: 1.61 ± 0.06 in control, 1.31 ± 0.09 in CPSN-sus, 1.02 ± 0.15 in CNBS) (Fig. 5g). These data suggested a strong cardioprotection capacity of the CNBS patch against MI.

3.5. Immune environment modulated by CNBS patch

With a rat MI model, we confirmed that the CNBS patch played a great role in the regulation of inflammatory responses. Fluorescent images revealed the decreased infiltration of CD45-positive leukocytes around the site of infarction region after interventional treatment compared to the no-treatment control group (Fig. 6a and b). In addition, we speculated that compared to CPSN-sus, the immune response activated by foreign body was also mitigated by CNBS. The expression of CD68 protein in CNBS group was significantly downregulated compared to the CPSN-sus and no-treatment control groups, indicating the decrease of macrophages (Fig. 6c and d). To determine whether the macrophage polarization was regulated by the CNBS patch, we

conducted IHF staining against IL-1β (marker of pro-inflammatory M1 macrophages) and CD163 (marker of anti-inflammatory M2 macrophages). The results showed that after the treatment with CNBS, the expression of IL-1β was remarkably decreased while the expression of CD163 was elevated (Fig. 6e and f). More importantly, the ratio of CD163 to IL-1β in CNBS group was dramatically higher than those in CPSN-sus or no-treatment group (Figure s9b). The CNBS-treated rat hearts showed decreased IL-1β and TNF-α mRNA expressions, while the expression of anti-inflammatory IL-10 mRNA was significantly upregulated (Fig. 6g). Besides, the results of ELISA assay showed that MI caused a general increase in rat serum inflammatory factors (IL-8, TNF-α and IL-10), which was significantly reduced upon treatment with the CNBS patch (Fig. 6h). More importantly, the lower expression of anti-inflammatory IL-10 protein suggested the decreased inflammatory responses and a more advanced tissue remodeling stage of CNBS-treated rat hearts. Overall, these data indicated that CNBS treatment directed macrophages towards M2 polarization, thereby creating an immune-reparative environment for tissue regeneration.

3.6. Myocardial remodeling upon treatment with CNBS patch

The reparative effect of CNBS on myocardial remodeling was further assessed in the rat MI model. Compared with normal rat hearts, we observed the depressed CX43 in infarction regions (Fig. 7a and Figure s10a and b). Interestingly, the limited CX43 in CPSN-sus group presented disordered localization with lateral orientation. By contrast, the CNBS-treated rat hearts exhibited relatively structural gap junctions and myocardial alignment (Fig. 7b and c). In agreement with this, the MI-injured rat hearts showed disrupted N-cadherin organization and suppressed cTnT expression even upon treatment with CPSN-sus, which was rescued upon treatment with the CNBS patch (Fig. 7d–f and Figure s10c and d). We assumed that the superior myocardial remodeling effects of CNBS were attributed to the improved gap junction reconstruction and the successive electromechanical coupling between cardiac myocytes in the peri-infarct zone.

Because reactivating cardiomyocyte renewal capacity in mature mammalian hearts is a therapeutically promising approach for cardiac regeneration post MI injury, we examined cardiomyocyte proliferation by ki67 staining. After 28 days, MI injury induced a decrease in ki67-positive cardiomyocytes compared to sham. Fluorescent images revealed increased ki67 levels in rat hearts upon treatment with CPSN-sus or CNBS, as well as a stronger fluorescent signal in the latter (Fig. 7g–i). Even it was not clear whether cardiomyocyte renewal originated from the host cells or exogenous BADSCs, the above results suggested CNBS treatment was beneficial in promoting cardiomyocyte renewal.

Myocardial revascularization is also necessary for rescuing the infarcted myocardium. The neovascularization after 28 days was detected by IHF staining against CD34, a surface marker of hematopoietic progenitor cells and blood vessel endothelial cells. CNBS significantly upregulated the expression of CD34 compared with CPSN-sus and the control groups (Fig. 8a and b). IHF staining with α-SMA, a marker of vascular smooth muscle cells, further confirmed the neovascularization in rat hearts. The results showed that the number of α-SMA-positive blood vessels in the CNBS group was significantly higher than in the CPSN-sus and control group (Fig. 8c and d). Finally, we performed a doppler ultrasound assay to evaluate cardiac functions after 4 weeks of treatments (Fig. 8e). The rat infarcted hearts exhibited typical
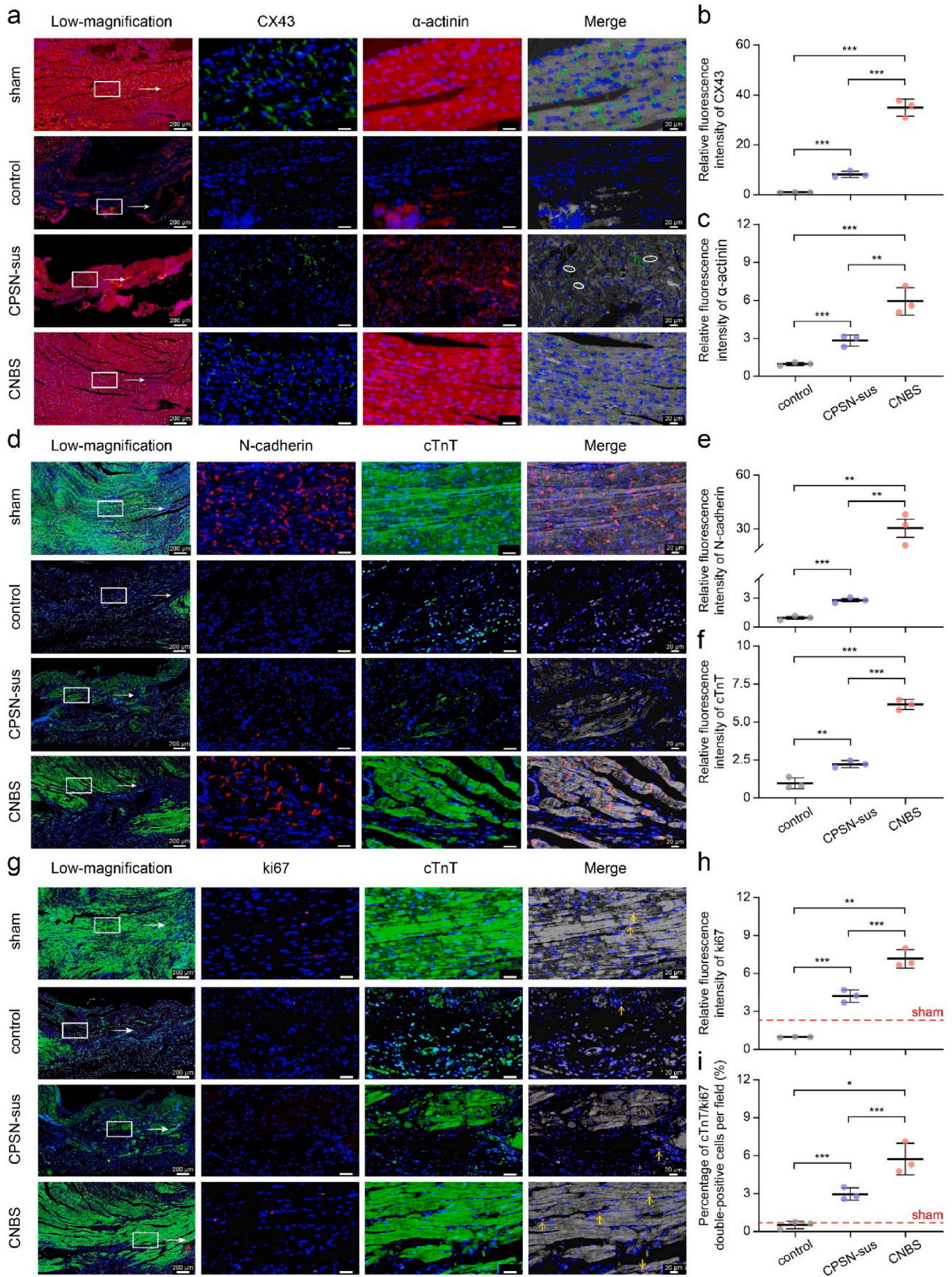
(caption on next page)

Fig. 7. CNBS patch restored myocardial structures and promoted cardiomyocyte renewal in rat hearts. (a–c) Representative confocal images showing cardiomyocyte α-actinin (red) and CX43 (green)-positive gap junctions with white arrows indicating the lateral CX43 orientation. (d–f) Cell-to-cell adhesion was revealed by immunostaining against N-cadherin (red) and mature cardiomyocyte marker cTnT (green), and the fold change in fluorescence intensity was quantified accordingly. (g–i) Cardiomyocyte proliferation was detected by immunostaining against ki67 (red) and cTnT (green), and the cTnT/ki67 double-positive cardiomyocytes (indicated by yellow arrows) were quantified. For (a, d, and g), the nucleus was counterstained by DAPI (blue). In the merge images, fluorescences of cardiomyocyte markers α-actinin and cTnT were greyed out to better manifest gap junction markers CX43 and N-cadherin and cell proliferation marker ki67. For (b, c, e and f), data for the sham group were not presented because they were exclusively large. *, $p < 0.05$; **, $p < 0.01$; ***, $p < 0.001$; ****, $p < 0.0001$ according to one-way ANOVA followed by LSD post-hoc test (b, c, e, f, h and i). All data were shown as mean $\pm$ SD. Values of independent experiments were: n = 3 (b, c, e, f, h and i).

MI features with a notable reduction in LVEF and LVFS. The rat hearts that received CPSN-sus treatments displayed significantly increased LVEF and LVFS. The therapeutic efficiency was further amplified by CNBS patch, which were comparable to previous reports (Fig. 8f and g) [50]. Simultaneously, the rats transplanted with CNBS patch were found to have the lowest EDV and ESV, demonstrating a relatively healthy cardiac function (Fig. 8h and i). It was desirable that the supplemental BADSCs differentiated into cardiomyocyte-like cells, favoring the remodeling of the functional myocardium.

4. Discussion

Despite wide reports in tissue engineering, the limited physical properties of cell sheets still challenge their advanced applications in the treatments for MI [51]. The in vivo preservation is another acknowledged challenge for cell-based therapy [52,53]. Here, we developed a biomaterial-cell sheet system to treat MI, in which CPSN was designed to enhance the mechanical strength while BADSCs sheet provided reparative effects. After investigating the benefits of CPSN in vitro, the in vivo therapeutic efficiency of CNBS patch was further evaluated in a rat MI model.

SF is one of the most promising biomaterials due to its biocompatibility and biodegradability. Different from previously reported material, it is most recently reported that SF possesses the potential to convert quiescent ventricular cardiomyocytes into pacemaker cardiomyocytes, which further consolidates the versatility and acknowledgment of SF to treat heart diseases [31,54]. Our data showed an enhanced cardiac differentiation of BADSCs cultured on the CPSN substrate compared to those cultured on normal Petri dish. Considering the limited elongation rate of SF, we chose electrospun PSN as a substrate, trying to meet the mechanical requirements for systolic and diastolic functions of heart tissues [55]. A relatively low Young's modulus of the cardiac patch would allow its deformation with heart beating [56]. In our study, Young's modulus of PSN was about 12.38 ± 1.83 MPa, which was closer to the reported value of heart tissues compared with electrospun SF nanofibers (25.5 ± 1.89 MPa) [57]. Carefully screening the mechanical properties of the CNBS constructs will benefit their performance for in vivo cardiac remodeling. However, it is challenging to reproduce the mechanical properties of human muscle using artificial materials. Thus, there is still great room to optimize the mechanical properties of biomaterial cardiac patches. Meanwhile, due to large capacitive currents, the impedance of both bare PSN and CPSN decreased with the increase of frequency. We observed a markedly lower impedance of CPSN than that of bare PSN in the low-frequency range, which was comparable to previous studies [32]. The data revealed an enhanced electrical conductivity of electrospun nanofibers due to the addition of CNTs. More importantly, a strong α-actinin/CX43 double positive staining was observed for BADSCs cultured on the surface of CPSN, revealing that CPSN held great potential to support the differentiation of BADSCs towards cardiomyocytes. In contrast with the beating of cell aggregation in the control group, the BADSCs cultured on CPSN showed a more advanced contraction (video s1-s6). Notably, the rat BADSCs failed to differentiate into cardiomyocytes even after one passage without further treatment. However, the detailed mechanisms remain elusive. Nevertheless, desirable cell adhesion may contribute to the differentiation process. The porosity of electrospun nanofibers could also help preserve living cells or bio-functional cargoes around the damaged area and allow the integrity between nanofibers and host tissues [58].

Blending with conductive CNTs has been reported to help establish electrical activity between the infarcted region and healthy myocardium [32]. Our data supported the fact that intracellular calcium concentration was increased by the CPSN substrate (Fig. 2j-l), which was also confirmed by the upregulated expressions of MEF2C (Fig. 2d and f) and N-cadherin protein (Fig. 7d–f). Although we did not definitely explore the interactions between the biological factors and substrates, it still could be concluded that intracellular calcium flux and subsequent activation of transcriptional factors underlay the mechanism for cardiomyogenesis.

Unlike cell suspension, cell sheet engineering can reserve a relatively intact extracellular matrix, thus facilitating the growth and proliferation of surrounding cells by paracrine effects. With CNBS patch, we observed a significant increase for in vivo cell retention and stability. Our data suggested a more positive role of the CNBS patch than the CPSN-sus in regard of promoting cardiac revacularization, improving cardiomyocyte renewal, and reducing cell apoptosis. Although it is controversial how to effectively maintain enough cell survival in the core of multilayered cell sheets [15], there were still a large number of living cells after transplantation into rats for 4 weeks. More importantly, we confirmed the augmented myocardial regeneration in the infarcted area and inside of the transplanted CNBS patch.

Angiogenesis and inflammation are two natural mechanisms to restore the perfusion of infarcted myocardium and regulate a wide range of cellular processes followed by injury of MI [59–61]. We investigated the effects of CNBS patch on angiogenesis both in vitro and in vivo. The results suggested a positive role of CNBS patch in pro-angiogenesis. In cell migration experiments, our data supported an enhanced HUVECs migration when cultured with CNBS-CM, which was assumed to be ascribed to the abundance of pro-angiogenic and pro-migratory cytokines and factors from the BADSCs sheets. Besides, cell adhesion is strictly related to cell motility. Consistent with previous reports [62,63], we also demonstrated that the CPSN substrates upregulated the expression of gap junction proteins VE-cadherin (Fig. 2g and Figure s3) and N-cadherin (Fig. 7d). Then, the cells have more adhesive anchors, thereby improving cell motility. Besides, N-cadherin has been reported to upregulate the expressions of vascular endothelial growth factor (VEGF) through activating extracellular signal-regulated kinases (ERK) signaling pathway [64]. It might account for the enhanced cardiac revascularization upon treatment with CNBS patch. On the other hand, the blocked coronary arteries, which suffered from ischemia and hypoxia, is highly related to local inflammation. Danger factors released from necrotic cardiomyocytes will provoke an intense inflammatory response and result in the infiltration of CD68-positive macrophages. BADSCs can modulate the blood microenvironment and maintain surrounding cell survival through paracrine effects [65]. It is well known that classically activated macrophages (M1 macrophages) promote inflammation, extracellular matrix destruction, and cell apoptosis, while alternatively activated macrophages (M2 macrophages) contribute to tissue remodeling and angiogenesis [66]. M2 macrophages have been proven to secrete anti-inflammatory mediators and angiogenic factors. We also confirmed that CNBS patch upregulated M2 macrophage polarization through immunostaining and RT-PCR assay. In addition, the transplantation of biomaterial will definitely provoke foreign body response, resulting in the infiltration of leukocytes and activating
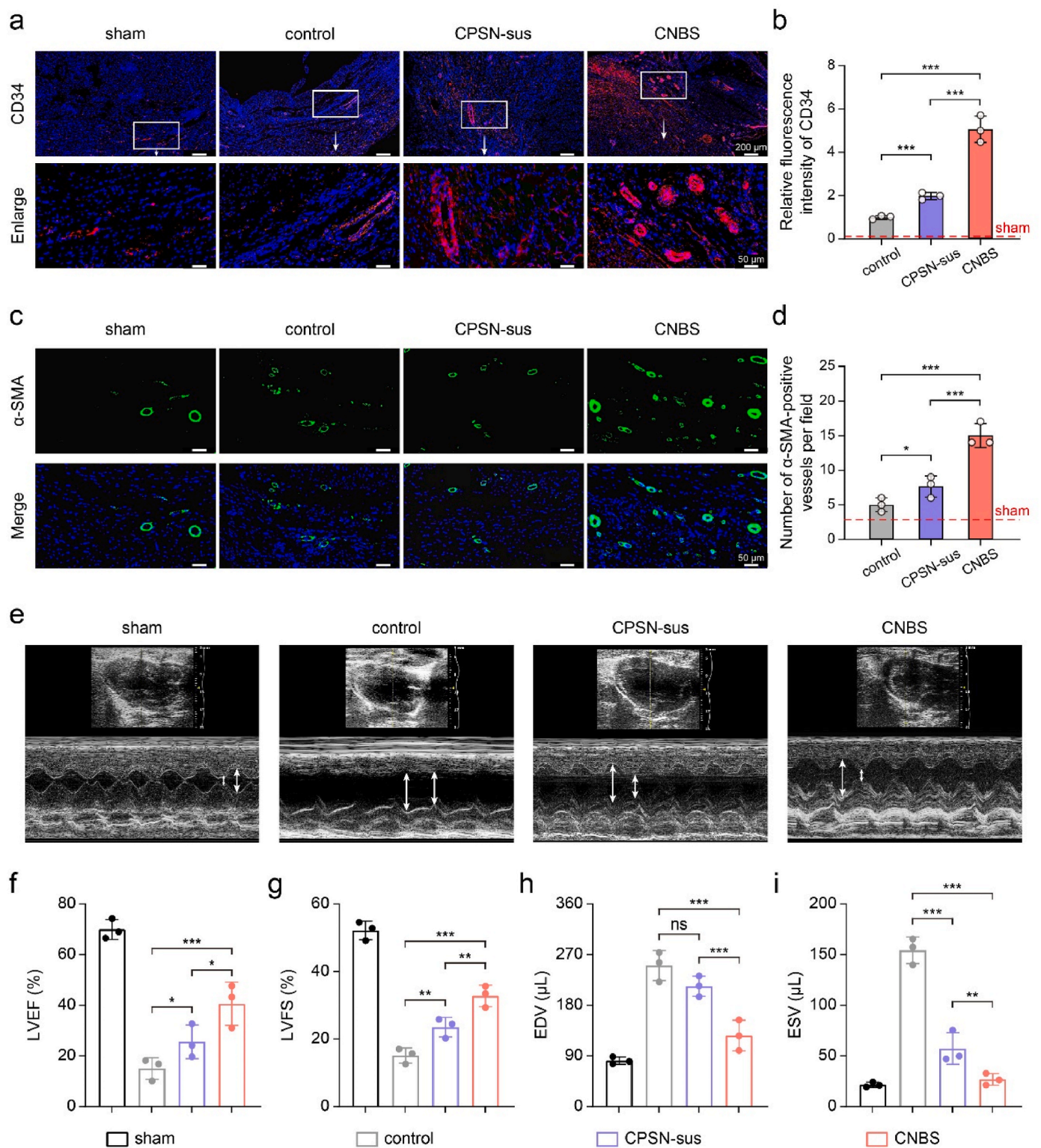
Fig. 8. CNBS patch treatment ameliorated ventricular dysfunction. (a and b) Neovascularization was assessed by immunostaining against CD34 (red), and the relative expression of CD34 was quantified accordingly. (c and d) Representative immunostaining images with α-SMA (green) and quantification of α-SMA-positive arterioles. (e) Representative M-mode echocardiography images showing cardiac function. (f–i) Left ventricular-ejection fractions (LVEF), fraction shortening (LVFS), volume at diastole (ESV), and end diastolic volume (EDV) were assessed accordingly. For (a and c), the nucleus was counterstained by DAPI (blue). *, $p < 0.05$; **, $p < 0.01$; ***, $p < 0.001$; ****, $p < 0.0001$ according to one-way ANOVA followed by LSD post-hoc test (b, d, and f-i). All data were shown as mean ± SD. Values of independent experiments were: n = 3 (b, d, and f-i).

inflammation [67]. Immunostaining showed a decrease of CD45-positive leukocytes and CD68-positive macrophages with CNBS treatment, suggesting a positive role of CNBS in M2 macrophage polarization and tissue remodeling (Fig. 6). Therefore, we concluded that the CNBS patch exerted a composite effect on skewing reparative macrophage polarization and promoting angiogenesis, thereby accelerating cardiac remodeling.

The aforementioned effects of CNBS patch accounted for the recovery of cardiac functions. It has reached a consensus that effective heart regeneration after injury benefits from cardiomyocyte renewal. The addition of pluripotent stem cell-derived cardiomyocyte grafts can revascularize and renovate infarcted myocardium through cardiomyocyte renewal [68]. With the great promises of BADSCs, CNBS patch created a favorable microenvironment for cardiac remodeling. The enlargement of the LV cavity was prevented by the CNBS patch. Likewise, a high level of CX43 and cTnT expression in the CNBS patch group indicated the advanced remodeling of gap junctions between cardiomyocytes, which is an exclusive feature of healthy myocardium [69]. However, the underlying mechanisms of such effects remain elusive. Several external cues, such as TBX18 gene transduction and trichostatin A stimulation, have been proposed for enhancing the differentiation of BADSCs into cardiomyocyte-like cells [70,71].

In light of the applications of synthetic polymers and natural materials in the treatments for cardiovascular diseases, we foresee the combination of biomaterial substrate and stem cell sheet engineering as a promising solution in acute MI. However, there are limitations to our study. First, the in vivo imaging for cell retention is relatively macroscopic and concealed. Colocalization of the rat cardiomyocytes and exogenous DiD-labeled BADSCs using immunofluorescence staining and long-term follow-up tracing of the transplanted BADSCs are needed to fully determine the in vivo cell retention. Meanwhile, biodegradability is critical to the long-term performance of cardiac patches. Studying the in vivo degradation of the CNBS will be useful to better understand the interactions between the CNBS patch and host hearts. Second, with an acute MI model, we fail to evaluate inflammatory responses at the early stage, while the final results are in line with those data from in vitro experiments and previous reports [5,50]. Third, screening the different ratios of each component (PCL, SF and CNTs) for fabricating the CPSN substrates will benefit therapeutic efficacy of the CNBS patch, which is also lost in the present study. It has been accepted that conductive CNTs have abilities to mimic the Purkinje network and have been well-studied in previous reports [32,72]. Therefore, we did not focus much on the functional assessments of CNTs, which should be paid attention to in the future study. Finally, transplanting the CNBS patch into large animals (e. g., pigs and rabbits) will be more precise to mimic the clinical scenarios. Nevertheless, the present study showed the potential therapeutic effects of using CNBS cardiac patches for myocardial remodeling as a pilot study.

5. Conclusions

In summary, we proposed, fabricated, and evaluated a biocompatible cardiac patch that could restore cardiac functions post-MI. Incorporating CNTs enabled the CNBS patch to keep high electrical conductivity. It was demonstrated that the CNBS cardiac patches could improve the retention and stability of BADSCs more than their suspension counterparts. The in vitro experiments revealed augmented angiogenesis and reduced inflammatory responses treated with the CNBS patch. Furthermore, the enhanced cardiac remodeling capacity of CNBS treatment was demonstrated by the repair of cardiomyocyte gap junctions (CX43 and N-cadherin) and the remodeling of myocardium structures (cTnT and α-actinin). In addition to the reduction of fibrotic regeneration, BADSCs-derived cardiomyocytes could also promote cardiac functions. Altogether, the present study showed the potential therapeutic efficiency of combining biomaterial substrate and cell sheets for restoring myocardium after ischemic MI.

Ethics approval and consent to participate

CRediT authorship contribution statement

Xinbo Wei: Conceptualization, Methodology, Software, and, Writing – original draft, preparation. **Li Wang:** Data curation, Methodology, and, Writing – original draft, preparation. **Cuimi Duan:** Conceptualization, and, Methodology. **Kai Chen:** Methodology. **Xia Li:** Conceptualization. **Ximin Guo:** Resources, and, Supervision. **Peng Chen:** Resources, and, Formal analysis. **Haifeng Liu:** Funding acquisition, Writing – review & editing, and, Supervision. **Yubo Fan:** Funding acquisition.

Acknowledgements

Abbreviations

PSN	electrospun PCL/SF nanofibers
CPSN	CNTs-containing PSN
CNBS	CPSN-BADSCs sheets
CPSN-sus	CPSN combined with BADSCs suspension
CNBS-CM	CNBS-derived conditioned media

Appendix A. Supplementary data

Supplementary data to this article can be found online at https://doi.org/10.1016/j.bioactmat.2023.03.023.

References

[1] M.D. Samsky, D.A. Morrow, A.G. Proudfoot, J.S. Hochman, H. Thiele, S.V. Rao, Cardiogenic shock after acute myocardial infarction: a review, JAMA 326 (2021) 1840–1850, https://doi.org/10.1001/jama.2021.18323.

[2] A.A. Damluji, S. van Diepen, J.N. Katz, V. Menon, J.E. Tamis-Holland, M. Bakitas, M.G. Cohen, L.B. Balsam, J. Chikwe, On behalf of the American heart association council on clinical cardiology; council on arteriosclerosis, thrombosis and vascular biology; council on cardiovascular surgery and anesthesia; and council on cardiovascular and stroke nursing, mechanical complications of acute myocardial infarction: a scientific statement from the American heart association, Circulation 144 (2021), https://doi.org/10.1161/CIR.0000000000000985.

[3] A.C. Fanaroff, S. Garcia, J. Giri, Myocardial infarction during the COVID-19 pandemic, JAMA 326 (2021), https://doi.org/10.1001/jama.2021.19608, 1916.

[4] M.C. Badescu, M. Ciocoiu, E. Rezus, O.V. Badulescu, D.M. Tanase, A. Ouatu, N. Dima, A.R. Ganceanu-Rusu, D. Popescu, P.N. Seritean Isac, T.-M. Genes, C. Rezus, Current therapeutic approach to acute myocardial infarction in patients with congenital hemophilia, Life 11 (2021) 1072, https://doi.org/10.3390/life11101072.

[5] K. Huang, E.W. Ozpinar, T. Su, J. Tang, D. Shen, L. Qiao, S. Hu, Z. Li, H. Liang, K. Mathews, V. Scharf, D.O. Freytes, K. Cheng, An off-the-shelf artificial cardiac patch improves cardiac repair after myocardial infarction in rats and pigs, Sci. Transl. Med. 12 (2020), eaat9683, https://doi.org/10.1126/scitranslmed.aat9683.

[6] R. Guo, F. Wan, M. Morimatsu, Q. Xu, T. Feng, H. Yang, Y. Gong, S. Ma, Y. Chang, S. Zhang, Y. Jiang, H. Wang, D. Chang, H. Zhang, Y. Ling, F. Lan, Cell sheet formation enhances the therapeutic effects of human umbilical cord mesenchymal stem cells on myocardial infarction as a bioactive material, Bioact. Mater. 6 (2021) 2999–3012, https://doi.org/10.1016/j.bioactmat.2021.01.036.

[7] S.E. Senyo, M.L. Steinhauser, C.L. Pizzimenti, V.K. Yang, L. Cai, M. Wang, T.-D. Wu, J.-L. Guerquin-Kern, C.P. Lechene, R.T. Lee, Mammalian heart renewal by pre-existing cardiomyocytes, Nature 493 (2013) 433–436, https://doi.org/10.1038/nature11682.

[8] K. Gabisonia, G. Prosdocimo, G.D. Aquaro, L. Carlucci, L. Zentilin, I. Secco, H. Ali, L. Braga, N. Gorgodze, F. Bernini, S. Burchielli, C. Collesi, L. Zandonà, G. Sinagra, M. Piacenti, S. Zacchigna, R. Bussani, F.A. Recchia, M. Giacca, MicroRNA therapy stimulates uncontrolled cardiac repair after myocardial infarction in pigs, Nature 569 (2019) 418–422, https://doi.org/10.1038/s41586-019-1191-6.

[9] G. Yang, Q. Chen, D. Wen, Z. Chen, J. Wang, G. Chen, Z. Wang, X. Zhang, Y. Zhang, Q. Hu, L. Zhang, Z. Gu, A therapeutic microneedle patch made from hair-derived keratin for promoting hair regrowth, ACS Nano 13 (2019) 4354–4360, https://doi.org/10.1021/acsnano.8b09573.

[10] Q. Hu, W. Sun, J. Wang, H. Ruan, X. Zhang, Y. Ye, S. Shen, C. Wang, W. Lu, K. Cheng, G. Dotti, J.F. Zeidner, J. Wang, Z. Gu, Conjugation of haematopoietic stem cells and platelets decorated with anti-PD-1 antibodies augments anti-leukaemia efficacy, Nat Biomed Eng 2 (2018) 831–840, https://doi.org/10.1038/s41551-018-0310-2.

[11] R. Sharma, V. Khristov, A. Rising, B.S. Jha, R. Dejene, N. Hotaling, Y. Li, J. Stoddard, C. Stankewicz, Q. Wan, C. Zhang, M.M. Campos, K.J. Miyagishima, D. McGaughey, R. Villasmil, M. Mattapallil, B. Stanzel, H. Qian, W. Wong, L. Chase, S. Charles, T. McGill, S. Miller, A. Maminishkis, J. Amaral, K. Bharti, Clinical-grade stem cell-derived retinal pigment epithelium patch rescues retinal degeneration in rodents and pigs, Sci. Transl. Med. 11 (2019), https://doi.org/10.1126/scitranslmed.aat5580 eaat5580.

[12] D. Zhu, Z. Li, K. Huang, T.G. Caranasos, J.S. Rossi, K. Cheng, Minimally invasive delivery of therapeutic agents by hydrogel injection into the pericardial cavity for cardiac repair, Nat. Commun. 12 (2021) 1412, https://doi.org/10.1038/s41467-021-21682-7.

[13] J. Tang, J. Wang, K. Huang, Y. Ye, T. Su, L. Qiao, M.T. Hensley, T.G. Caranasos, J. Zhang, Z. Gu, K. Cheng, Cardiac cell-integrated microneedle patch for treating myocardial infarction, Sci. Adv. 4 (2018), https://doi.org/10.1126/sciadv.aat9365 eaat9365.

[14] L. Gao, Z.R. Gregorich, W. Zhu, S. Mattapally, Y. Oduk, X. Lou, R. Kannappan, A. V. Borovjagin, G.P. Walcott, A.E. Pollard, V.G. Fast, X. Hu, S.G. Lloyd, Y. Ge, J. Zhang, Large cardiac muscle patches engineered from human induced-pluripotent stem cell–derived cardiac cells improve recovery from myocardial infarction in swine, Circulation 137 (2018) 1712–1730, https://doi.org/10.1161/CIRCULATIONAHA.117.030785.

[15] J. Yang, M. Yamato, C. Kohno, A. Nishimoto, H. Sekine, F. Fukai, T. Okano, Cell sheet engineering: recreating tissues without biodegradable scaffolds, Biomaterials 26 (2005) 6415–6422, https://doi.org/10.1016/j.biomaterials.2005.04.061.

[16] P. Menasché, Cell therapy trials for heart regeneration — lessons learned and future directions, Nat. Rev. Cardiol. 15 (2018) 659–671, https://doi.org/10.1038/s41569-018-0013-0.

[17] C.P. Hodgkinson, A. Bareja, J.A. Gomez, V.J. Dzau, Emerging concepts in paracrine mechanisms in regenerative cardiovascular medicine and biology, Circ. Res. 118 (2016) 95–107, https://doi.org/10.1161/CIRCRESAHA.115.305373.

[18] J.S. Burchfield, S. Dimmeler, Role of paracrine factors in stem and progenitor cell mediated cardiac repair and tissue fibrosis, Fibrogenesis Tissue Repair 1 (2008) 4, https://doi.org/10.1186/1755-1536-1-4.

[19] T. Shimizu, H. Sekine, Y. Isoi, M. Yamato, A. Kikuchi, T. Okano, Long-term survival and growth of pulsatile myocardial tissue grafts engineered by the layering of cardiomyocyte sheets, Tissue Eng. 12 (2006) 499–507, https://doi.org/10.1089/ten.2006.12.499.

[20] Q. Huang, Y. Zou, M.C. Arno, S. Chen, T. Wang, J. Gao, A.P. Dove, J. Du, Hydrogel scaffolds for differentiation of adipose-derived stem cells, Chem. Soc. Rev. 46 (2017) 6255–6275, https://doi.org/10.1039/c6cs00052e.

[21] T.T. Tran, C.R. Kahn, Transplantation of Adipose Tissue and Adipose-Derived Stem Cells as a Tool to Study Metabolic Physiology and for Treatment of Disease, 2015, p. 31.

[22] M. Horckmans, M. Bianchini, D. Santovito, R.T.A. Megens, J.-Y. Springael, I. Negri, M. Vacca, M. Di Eusanio, A. Moschetta, C. Weber, J. Duchene, S. Steffens, Pericardial adipose tissue regulates granulopoiesis, fibrosis, and cardiac function after myocardial infarction, Circulation 137 (2018) 948–960, https://doi.org/10.1161/CIRCULATIONAHA.117.028833.

[23] C.-F. Weng, C.-F. Wu, S.-H. Kao, J.-C. Chen, H.-H. Lin, Down-regulation of miR-34a-5p potentiates protective effect of adipose-derived mesenchymal stem cells against ischemic myocardial infarction by stimulating the expression of C1q/tumor necrosis factor-related protein-9, Front. Physiol. (2019) 10. https://www.frontiersin.org/articles/10.3389/fphys.2019.01445. (Accessed 11 July 2022).

[24] H. Lu, F. Wang, H. Mei, S. Wang, L. Cheng, Human adipose mesenchymal stem cells show more efficient angiogenesis promotion on endothelial colony-forming cells than umbilical cord and endometrium, Stem Cell. Int. (2018), 7537589, https://doi.org/10.1155/2018/7537589, 2018.

[25] T. Teshima, Y. Yuchi, R. Suzuki, H. Matsumoto, H. Koyama, Immunomodulatory effects of canine adipose tissue mesenchymal stem cell-derived extracellular vesicles on stimulated CD4+ T cells isolated from peripheral blood mononuclear cells, 2021, J Immunol Res (2021), 2993043, https://doi.org/10.1155/2021/2993043.

[26] Y. Zhu, T. Liu, K. Song, R. Ning, X. Ma, Z. Cui, ADSCs differentiated into cardiomyocytes in cardiac microenvironment, Mol. Cell. Biochem. 324 (2009) 117–129, https://doi.org/10.1007/s11010-008-9990-3.

[27] W. Wystrychowski, B. Patlolla, Y. Zhuge, E. Neofytou, R.C. Robbins, R.E. Beygui, Multipotency and cardiomyogenic potential of human adipose-derived stem cells from epicardium, pericardium, and omentum, Stem Cell Res. Ther. 7 (2016) 84, https://doi.org/10.1186/s13287-016-0343-y.

[28] V. Planat-Bénard, C. Menard, M. André, M. Puceat, A. Perez, J.-M. Garcia-Verdugo, L. Pénicaud, L. Casteilla, Spontaneous cardiomyocyte differentiation from adipose

[29] S. Masuda, T. Shimizu, M. Yamato, T. Okano, Cell sheet engineering for heart tissue repair, Adv. Drug Deliv. Rev. 60 (2008) 277–285, https://doi.org/10.1016/j.addr.2007.08.031.

[30] Y. Feng, G. Zhao, M. Xu, X. Xing, L. Yang, Y. Ma, M. Qi, X. Zhang, D. Gao, rGO/silk fibroin-modified nanofibrous patches prevent ventricular remodeling via yap/taz-TGFβ1/smads signaling after myocardial infarction in rats, Front. Cardiovasc. Med. 8 (2021), 718055, https://doi.org/10.3389/fcvm.2021.718055.

[31] Y.-F. Hu, A.-S. Lee, S.-L. Chang, S.-F. Lin, C.-H. Weng, H.-Y. Lo, P.-C. Chou, Y.-N. Tsai, Y.-L. Sung, C.-C. Chen, R.-B. Yang, Y.-C. Lin, T.B.J. Kuo, C.-H. Wu, J.-D. Liu, T.-W. Chung, S.-A. Chen, Biomaterial-induced conversion of quiescent cardiomyocytes into pacemaker cells in rats, Nat. Biomed. Eng. 6 (2022) 421–434, https://doi.org/10.1038/s41551-021-00812-y.

[32] L. Wang, Injectable and conductive cardiac patches repair infarcted myocardium in rats and minipigs, Nature Biomedical Engineering 5 (2021) 20.

[33] L. Li, Y. Liu, C. Song, S. Sheng, L. Yang, Z. Yan, D.J.J. Hu, Q. Sun, Wearable alignment-free microfiber-based sensor chip for precise vital signs monitoring and cardiovascular assessment, Adv. Fiber Mater. 4 (2022) 475–486, https://doi.org/10.1007/s42765-021-00121-8.

[34] T. Nezakati, A. Seifalian, A. Tan, A.M. Seifalian, Conductive polymers: opportunities and challenges in biomedical applications, Chem. Rev. 118 (2018) 6766–6843, https://doi.org/10.1021/acs.chemrev.6b00275.

[35] M. Barrejón, S. Marchesan, N. Alegret, M. Prato, Carbon nanotubes for cardiac tissue regeneration: state of the art and perspectives, Carbon 184 (2021) 641–650, https://doi.org/10.1016/j.carbon.2021.08.059.

[36] Y. Zhao, Z. Zhang, Z. Pan, Y. Liu, Advanced bioactive nanomaterials for biomedical applications, Explorations 1 (2021), 20210089, https://doi.org/10.1002/EXP.20210089.

[37] J. Ren, Q. Xu, X. Chen, W. Li, K. Guo, Y. Zhao, Q. Wang, Z. Zhang, H. Peng, Y.-G. Li, Superaligned carbon nanotubes guide oriented cell growth and promote electrophysiological homogeneity for synthetic cardiac tissues, Adv. Mater. 29 (2017), 1702713, https://doi.org/10.1002/adma.201702713.

[38] Y. Chen, X. Dong, M. Shafiq, G. Myles, N. Radacsi, X. Mo, Recent advancements on three-dimensional electrospun nanofiber scaffolds for tissue engineering, Adv. Fiber Mater 4 (2022) 959–986, https://doi.org/10.1007/s42765-022-00170-7.

[39] X. Wan, Y. Zhao, Z. Li, L. Li, Emerging polymeric electrospun fibers: from structural diversity to application in flexible bioelectronics and tissue engineering, Explorations 2 (2022), 20210029, https://doi.org/10.1002/EXP.20210029.

[40] Z. Liu, H. Wang, Y. Zhang, J. Zhou, Q. Lin, Y. Wang, C. Duan, K. Wu, C. Wang, Efficient isolation of cardiac stem cells from Brown adipose, J. Biomed. Biotechnol. (2010) 1–9, https://doi.org/10.1155/2010/104296, 2010.

[41] B. Baudin, A. Bruneel, N. Bosselut, M. Vaubourdolle, A protocol for isolation and culture of human umbilical vein endothelial cells, Nat. Protoc. 2 (2007) 481–485, https://doi.org/10.1038/nprot.2007.54.

[42] Y.M. Efremov, I.M. Zurina, V.S. Presniakova, N.V. Kosheleva, D.V. Butnaru, A. A. Svistunov, Y.A. Rochev, P.S. Timashev, Mechanical properties of cell sheets and spheroids: the link between single cells and complex tissues, Biophys Rev 13 (2021) 541–561, https://doi.org/10.1007/s12551-021-00821-w.

[43] M.A. Nazeer, E. Yilgor, I. Yilgor, Electrospun polycaprolactone/silk fibroin nanofibrous bioactive scaffolds for tissue engineering applications, Polymer 168 (2019) 86–94, https://doi.org/10.1016/j.polymer.2019.02.023.

[44] C. Porter, Quantification of UCP1 function in human brown adipose tissue, Adipocyte 6 (2017) 167–174, https://doi.org/10.1080/21623945.2017.1319535.

[45] M.-C. Yang, S.-S. Wang, N.-K. Chou, N.-H. Chi, Y.-Y. Huang, Y.-L. Chang, M.-J. Shieh, T.-W. Chung, The cardiomyogenic differentiation of rat mesenchymal stem cells on silk fibroin–polysaccharide cardiac patches in vitro, Biomaterials 30 (2009) 3757–3765, https://doi.org/10.1016/j.biomaterials.2009.03.057.

[46] M. Hirata, T. Yamaoka, Effect of stem cell niche elasticity/ECM protein on the self-beating cardiomyocyte differentiation of induced pluripotent stem (iPS) cells at different stages, Acta Biomater. 65 (2018) 44–52, https://doi.org/10.1016/j.actbio.2017.10.032.

[47] H.-P. Chen, J. Wen, S.-R. Tan, L.-M. Kang, G.-C. Zhu, MiR-199a-3p inhibition facilitates cardiomyocyte differentiation of embryonic stem cell through promotion of MEF2C, J. Cell. Physiol. 234 (2019) 23315–23325, https://doi.org/10.1002/jcp.28899.

[48] B.J. van Meer, A. Krotenberg, L. Sala, R.P. Davis, T. Eschenhagen, C. Denning, L.G. J. Tertoolen, C.L. Mummery, Simultaneous measurement of excitation-contraction coupling parameters identifies mechanisms underlying contractile responses of hiPSC-derived cardiomyocytes, Nat. Commun. 10 (2019) 4325, https://doi.org/10.1038/s41467-019-12354-8.

[49] C. Communal, M. Sumandea, P. de Tombe, J. Narula, R.J. Solaro, R.J. Hajjar, Functional consequences of caspase activation in cardiac myocytes, Proc. Natl. Acad. Sci. U. S. A. 99 (2002) 6252–6256, https://doi.org/10.1073/pnas.092022999.

[50] R. Guo, F. Wan, M. Morimatsu, Q. Xu, T. Feng, H. Yang, Y. Gong, S. Ma, Y. Chang, S. Zhang, Y. Jiang, H. Wang, D. Chang, H. Zhang, Y. Ling, F. Lan, Cell sheet formation enhances the therapeutic effects of human umbilical cord mesenchymal stem cells on myocardial infarction as a bioactive material, Bioact. Mater. 6 (2021) 2999–3012, https://doi.org/10.1016/j.bioactmat.2021.01.036.

[51] R. Guo, M. Morimatsu, T. Feng, F. Lan, D. Chang, F. Wan, Y. Ling, Stem cell-derived cell sheet transplantation for heart tissue repair in myocardial infarction, Stem Cell Res. Ther. 11 (2020) 19, https://doi.org/10.1186/s13287-019-1536-y.

[52] H. Wang, J. Shi, Y. Wang, Y. Yin, L. Wang, J. Liu, Z. Liu, C. Duan, P. Zhu, C. Wang, Promotion of cardiac differentiation of brown adipose derived stem cells by

chitosan hydrogel for repair after myocardial infarction, Biomaterials 35 (2014) 3986–3998, https://doi.org/10.1016/j.biomaterials.2014.01.021.

[53] M.A. Thal, P. Krishnamurthy, A.R. Mackie, E. Hoxha, E. Lambers, S. Verma, V. Ramirez, G. Qin, D.W. Losordo, R. Kishore, Enhanced angiogenic and cardiomyocyte differentiation capacity of epigenetically reprogrammed mouse and human endothelial progenitor cells augments their efficacy for ischemic myocardial repair, Circ. Res. 111 (2012) 180–190, https://doi.org/10.1161/CIRCRESAHA.112.270462.

[54] S.H. Kim, Y.K. Yeon, J.M. Lee, J.R. Chao, Y.J. Lee, Y.B. Seo, MdT. Sultan, O.J. Lee, J.S. Lee, S. Yoon, I.-S. Hong, G. Khang, S.J. Lee, J.J. Yoo, C.H. Park, Precisely printable and biocompatible silk fibroin bioink for digital light processing 3D printing, Nat. Commun. 9 (2018) 1620, https://doi.org/10.1038/s41467-018-03759-y.

[55] T. Chang, Biomaterials based cardiac patches for the treatment of myocardial infarction, J. Mater. Sci. (2021) 13.

[56] K. Sim, F. Ershad, Y. Zhang, P. Yang, H. Shim, Z. Rao, Y. Lu, A. Thukral, A. Elgalad, Y. Xi, B. Tian, D.A. Taylor, C. Yu, An epicardial bioelectronic patch made from soft rubbery materials and capable of spatiotemporal mapping of electrophysiological activity, Nat Electron 3 (2020) 775–784, https://doi.org/10.1038/s41928-020-00493-6.

[57] D. Zhu, J. Hou, M. Qian, D. Jin, T. Hao, Y. Pan, H. Wang, S. Wu, S. Liu, F. Wang, L. Wu, Y. Zhong, Z. Yang, Y. Che, J. Shen, D. Kong, M. Yin, Q. Zhao, Nitrate-functionalized patch confers cardioprotection and improves heart repair after myocardial infarction via local nitric oxide delivery, Nat. Commun. 12 (2021) 4501, https://doi.org/10.1038/s41467-021-24804-3.

[58] S.B. Mahjour, F. Sefat, Y. Polunin, L. Wang, H. Wang, Improved cell infiltration of electrospun nanofiber mats for layered tissue constructs, J. Biomed. Mater. Res. 104 (2016) 1479–1488, https://doi.org/10.1002/jbm.a.35676.

[59] X. Wu, M.R. Reboll, M. Korf-Klingebiel, K.C. Wollert, Angiogenesis after acute myocardial infarction, Cardiovasc. Res. 117 (2021) 1257–1273, https://doi.org/10.1093/cvr/cvaa287.

[60] M. Oostendorp, K. Douma, A. Wagenaar, J.M.G.M. Slenter, T.M. Hackeng, M.A.M. J. van Zandvoort, M.J. Post, W.H. Backes, Molecular magnetic resonance imaging of myocardial angiogenesis after acute myocardial infarction, Circulation 121 (2010) 775–783, https://doi.org/10.1161/CIRCULATIONAHA.109.889451.

[61] A. Saxena, I. Russo, N.G. Frangogiannis, Inflammation as a therapeutic target in myocardial infarction: learning from past failures to meet future challenges, Transl. Res. 167 (2016) 152–166, https://doi.org/10.1016/j.trsl.2015.07.002.

[62] H. Ravanbakhsh, G. Bao, L. Mongeau, Carbon nanotubes promote cell migration in hydrogels, Sci. Rep. 10 (2020) 2543, https://doi.org/10.1038/s41598-020-59463-9.

[63] S.R. Shin, S.M. Jung, M. Zalabany, K. Kim, P. Zorlutuna, S.B. Kim, M. Nikkhah, M. Khabiry, M. Azize, J. Kong, K.-T. Wan, T. Palacios, M.R. Dokmeci, H. Bae, X.

S. Tang, A. Khademhosseini, Carbon-nanotube-embedded hydrogel sheets for engineering cardiac constructs and bioactuators, ACS Nano 7 (2013) 2369–2380, https://doi.org/10.1021/nn305559j.

[64] L. Ej, C. Ek, K. Sk, K. Gh, P. Jy, K. Hj, L. Sw, K. Kh, K. Js, L. Kh, A. Y, L. Hj, C. Hj, C. Sj, O. Wi, P. Yb, K. Hs, N-cadherin determines individual variations in the therapeutic efficacy of human umbilical cord blood-derived mesenchymal stem cells in a rat model of myocardial infarction, Mol. Ther. : The Journal of the American Society of Gene Therapy 20 (2012), https://doi.org/10.1038/mt.2011.202.

[65] J. Zhang, Y. Liu, Y. Chen, L. Yuan, H. Liu, J. Wang, Q. Liu, Y. Zhang, Adipose-derived stem cells: current applications and future directions in the regeneration of multiple tissues, Stem Cell. Int. (2020) 1–26, https://doi.org/10.1155/2020/8810813, 2020.

[66] T.A. Wynn, A. Chawla, J.W. Pollard, Macrophage biology in development, homeostasis and disease, Nature 496 (2013) 445–455, https://doi.org/10.1038/nature12034.

[67] A.E. Thurber, In Vivo Bioresponses to Silk Proteins, 2015, p. 13.

[68] Y.-W. Liu, B. Chen, X. Yang, J.A. Fugate, F.A. Kalucki, A. Futakuchi-Tsuchida, L. Couture, K.W. Vogel, C.A. Astley, A. Baldessari, J. Ogle, C.W. Don, Z. L. Steinberg, S.P. Seslar, S.A. Tuck, H. Tsuchida, A.V. Naumova, S.K. Dupras, M. S. Lyu, J. Lee, D.W. Hailey, H. Reinecke, L. Pabon, B.H. Fryer, W.R. MacLellan, R. S. Thies, C.E. Murry, Human embryonic stem cell–derived cardiomyocytes restore function in infarcted hearts of non-human primates, Nat. Biotechnol. 36 (2018) 597–605, https://doi.org/10.1038/nbt.4162.

[69] Y. Yao, Y. Ding, J. Zhang, Z. Wang, H. Zhang, J. Xie, Y. Wang, L. Hong, Z. Mao, J. Gao, C. Gao, ROS-responsive polyurethane fibrous patches loaded with methylprednisolone (MP) for restoring structures and functions of infarcted myocardium in vivo, Biomaterials 232 (2020), 119726, https://doi.org/10.1016/j.biomaterials.2019.119726.

[70] M. Yang, G.-G. Zhang, T. Wang, X. Wang, Y.-H. Tang, H. Huang, H. Barajas-Martinez, D. Hu, C.-X. Huang, TBX18 gene induces adipose-derived stem cells to differentiate into pacemaker-like cells in the myocardial microenvironment, Int. J. Mol. Med. 38 (2016) 1403–1410, https://doi.org/10.3892/ijmm.2016.2736.

[71] Z. Bagheri-Hosseinabadi, P. Salehinejad, S.A. Mesbah-Namin, Differentiation of human adipose-derived stem cells into cardiomyocyte-like cells in fibrin scaffold by a histone deacetylase inhibitor, Biomed. Eng. Online 16 (2017) 134, https://doi.org/10.1186/s12938-017-0423-y.

[72] W. Liang, J. Chen, L. Li, M. Li, X. Wei, B. Tan, Y. Shang, G. Fan, W. Wang, W. Liu, Conductive hydrogen sulfide-releasing hydrogel encapsulating ADSCs for myocardial infarction treatment, ACS Appl. Mater. Interfaces 11 (2019) 14619–14629, https://doi.org/10.1021/acsami.9b01886.